Classifying structural alterations of the cytoskeleton by spectrum enhancement and descriptor fusion

Giovanni F. Crosta
Chiara Urani
Laura Fumarola
Università degli Studi Milano–Bicocca
Department of Environmental Sciences
Inverse Problems and Mathematical Morphology Unit
1, Piazza della Scienza
I-20126 Milan, Italy
E-mail: Giovanni_Crosta@uml.edu

Abstract. A classifier capable of ranking structural alterations of the cytoskeleton is developed. Images of cytoskeletal microtubules obtained from the epifluorescence microscopy of primary culture rat hepatocytes are analyzed. Morphological descriptors are extracted by contour and mass fractal analysis, direct methods, and spectrum enhancement. All methods are designed and tuned to make the extracted morphological descriptors insensitive to absolute fluorescence intensities. Spectrum enhancement is a nonlinear filter that involves spatial differentiation of the gray-scale image followed by conversion of power spectral density to the logarithmic scale and averaging over arcs in the reciprocal domain. Enhanced spectra exhibit local maxima that correspond to the structured microtubule bundles of a normal cytoskeleton. Descriptor fusion for classification is achieved by means of multivariate analysis. The classifier is trained by image sets representing normal ("negative control") microtubules and those altered by exposure to a fungicide at the highest dose of the experiment design. Some sensitivity and validation tests, including discriminant functions analysis, are applied to the classifier. The latter is applied to recognize images of microtubules not used in the training stage and comes from treatments at lower concentrations and shorter times. As a result, structural alterations are ranked and structural recovery after treatment is quantified. The method has potential use in quantitative, morphology-based tests on the cytoskeleton treated either by anticancer drugs or by cytotoxic agents. © *2006 Society of Photo-Optical Instrumentation Engineers.* [DOI: 10.1117/1.2187423]

1 Introduction and Motivation

The automatic classification and recognition of images obtained from various microscopic applications is a task of paramount importance to disciplines ranging from materials science to cell biology. This paper focuses on the morphology of the cytoskeleton, made visible by epifluorescence microscopy, processed by some methods that extract features (morphological descriptors) and classified by means of multivariate statistics.

1.1 Cytoskeleton

The cytoskeleton is a network of proteins that structurally and dynamically organize the cytoplasm of living cells.[1] It is composed of three major structural elements: microtubules, intermediate filaments, and microfilaments, each consisting of polymers of protein subunits.

The cytoskeleton is responsible for the maintenance of cell architecture, shape, and internal organization. For example, it enables the transport of organelles and vescicles. Microtubules and actin filaments play a role in mitosis, cell signaling, and motility.[2]

A well-organized cytoskeletal network exhibits, as in the top tile of Fig. 1 and in Fig. 2, bundles of microtubules radiating from the microtubule organizing center (MTOC), located near the cell nucleus, toward the cell periphery.

In general, alterations of cytoskeletal functions are related to (may be the cause or the effect of) a broad spectrum of biochemical reactions such as adenosine triphosphate (ATP) depletion, disruption of intracellular ion (Ca^{2+}) homeostasis, thiol oxidation, and phosphorylation,[3–7] all of which have major repercussions on cell functionality. Many substances are known to directly or indirectly interact with cytoskeletal constituents and cause damage: metals,[8,9] herbicides and fungicides,[3,10] the neurotoxin[4] MPTP, as well as natural toxins.[5]

In morphological terms, damage to the microtubule network consists of structural disorganization, inhibition of assembly, disassembly, or depolymerization. All of these pat-

Address all correspondence to Giovanni F. Crosta, Environmental Sciences University Milan Bicocca 1, Piazza della Scienza MILAN, 20126 Italy. Tel: +390264482724. Fax: +390264482754. E-mail: Giovanni_Crosta@uml.edu
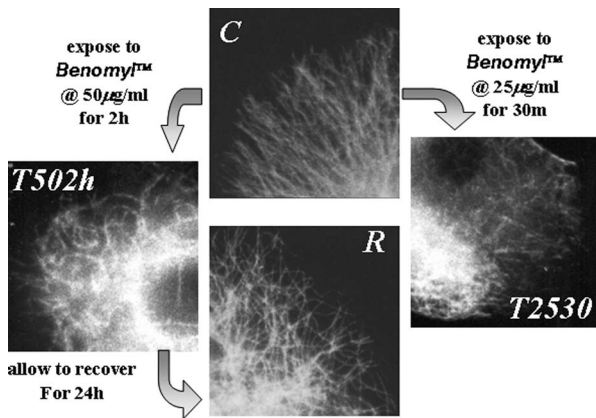
Fig. 1 Outline of the experiment design. All images show microtubules of cultured rate hepatocytes obtained by immunolocalization and epifluorescence microscopy. *C*, tile from the untreated (control) set; *T502h*, tile from treatment at the highest concentration (50 μg/ml) for the longest time (2 h); *R*; tile from the recovery experiment; and *T2530*; tile from an intermediate treatment. In tiles *T502h* and *T2530* the dark round area corresponds to the nucleus, in proximity of which the MTOC is located. Square side length=13 μm.

terns can be visualized by means of suitable techniques[11] (e.g., Sec. 3).

In turn, morphological alterations of the cytoskeleton reflect functional disturbances of the whole cell, e.g., altered transport of very low density lipoproteins in hepatocytes,[12] neurodegeneration,[13–15] and cell transformation.[16] For this last reason the cytoskeleton has become one of the preferred targets of anticancer drugs.[17–22]

Therefore cytoskeletal morphology is a valuable indicator of cell functionality. In this context, morphological analysis and classification of cytoskeletal images can assist in estimating the degree of cell injury.
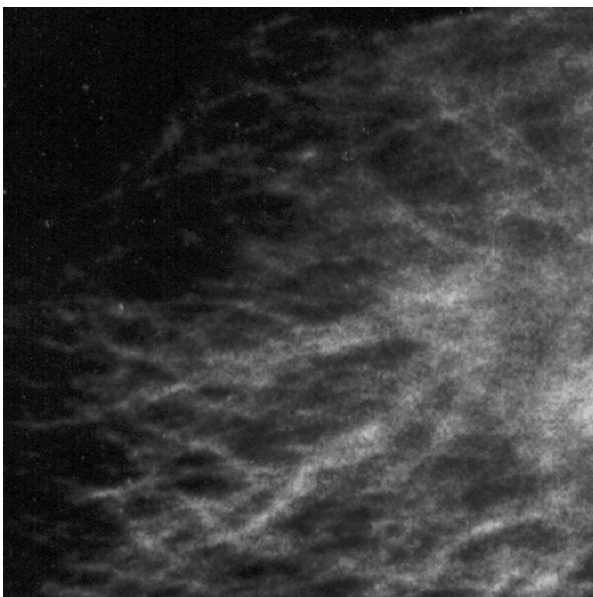

Fig. 2 Microtubules of a control cell, tile cont_03o. Square side length=13 μm.

1.2 Image Classification

Image classification can be either dichotomic or of "continuous" type. The former is meant to provide yes/no answers, the latter is expected to rank images according to some predefined properties. Moreover, image classification paradigms differ by the type of data processed. Raw images can be supplied as such to a black box algorithm, which is requested to sort out similarities and rank images accordingly.[23,24] Instead, the paradigm implemented in this paper starts with the extraction of a few quantitative morphological descriptors, also called indicators or features, believed to effectively translate structural, hence functional information. Features were extracted by the following methods: contour (Secs. 5.2 and 6.1) and mass fractal analysis (Secs. 5.3 and 6.2); spatial differentiation (Secs. 5.4 and 6.3); and "spectrum enhancement," a nonlinear filter in the Fourier domain (Secs. 5.5 and 6.4). Descriptor selection is based on known function-morphology relations and driven by the properties of the available images (Sec. 4.1).

Classification and quantitative assessment then relies on the four standard steps:

1. training on sets of images which represent extreme situations (Sec. 7)

2. sensitivity analysis with respect to control parameters and validation by the submission of new inputs (Sec. 8)

3. recognition of images coming from different experiments (Sec. 9),

4. image ranking by means of some numerical indicators, as required by the intended application (Sec. 9).

These stages are all reflected in the experiment design (Sec. 4) and the developments described in the following, where the eventual application is the quantitative description of cytoskeletal morphology affected by damage (Sec. 9.1) or undergoing recovery (Sec. 9.2).

2 Related Work

Very roughly speaking, mathematical models of the morphology and organization of the cytoskeleton have served two different purposes: either to simulate cytoskeletal dynamics or to analyze a specific process of interest. Although a comprehensive overview of prior work is beyond the scope of this paper, some results concerning modeling and simulation deserve to be mentioned, namely, those by Dufort and Lumsden,[25] who developed a cellular automaton model; by Edelstein-Keshet and Ermentrout,[26] who interpreted actin-filament length distribution in a lamellipodium; and by Aon and Cortassa,[27] who investigated the influence of cytoskeletal organization and dynamics on cell biochemistry. Moreover, fractal models have been proposed in a variety of situations involving the cytoskeleton.[28,29]

On the process analysis side, as early as 1992 and within a program aimed at extracting features from moving cells, Lifshitz[30] developed a microtubule tracking algorithm that relied on model matching, and Thomason et al.[31] related the mass fractal dimension to cytoskeleton rearrangement dynamics in cardiac muscle. Spatial differentiation and edge detection have been applied, e.g., by Karlon et al.,[32] who measured cell alignment and cytoskeletal organization by means of a gradient method; Knight et al.[33] applied a Sobel filter to obtain comprehensive results about the quantitative morphology

of cytoskeletal organization. Fourier analysis was used, e.g., by McGough and Josephs[34] to quantify the structure of erythrocyte spectrin and by Petroll et al.[35] to describe the orientation of stress fibers. To the best of our knowledge Kohler et al.[36] were the first to compare arc-averaged power spectral profiles of cytoskeletal images in the reciprocal domain. In fact, image comparison based on arc-averaged power spectra (improperly called "radially averaged") is a well-established procedure[37] derived from robust (rotation-invariant) target detection. Other methods of pattern analysis such as hierarchical feature vector matching have been applied to confocal microscope images of living cells to quantify cytoskeletal deformation.[38] More generally, the supervised or unsupervised classification and recognition of subcellular structures are strategic tasks in cell biology and proteomics,[39,40] which have far reaching consequences in diagnostics and health care.

This paper is an account of the results obtained so far by the authors. The earliest results appeared in some conference proceedings.[41–45]

3 Materials and Experimental Methods

Experiments that yielded the images of interest involved primary cultures of rat hepatocytes. The latter cells were obtained by the modified method of collagenase perfusion.[3] Male Sprague-Dawley rats (weighing 200 to 250 g) were anesthetized by intraperitoneal (ip) injection of 40 mg sodium penthobarbital/kg body weight. The abdomen, previously washed with alcohol, was opened and the portal vein cannulated, the liver was perfused with 50 ml Hank's balanced salt solution (HBSS)—Ca^{2+}-Mg^{2+} buffer (138 mM NaCl, 5.3 mM KCl, 0.33 mM $Na_2HPO_4 \cdot 2H_2O$, 0.44 mM KH_2PO_4, 5.5 mM glucose, 150 mM phenol red, 7.5% w/v $NaHCO_3$, pH 7.4) for 10 min and then for 15 min with 75 ml HBSS buffer containing collagenase (28 mg/8 ml medium). The liver was placed in a culture dish containing William's E medium (Sigma Chemical Company, St. Louis, Missouri, USA) supplemented with 0.2% bovine serum albumine (BSA), 10^{-7}-M dexamethasone, 10-μg/ml bovine pancreas insulin, and 50-μg/ml gentamycin sulphate and decapsulated. The suspension was filtered through cotton gauze and washed twice with culture medium by sedimentation. Cell viability was determined by trypan blue exclusion and was >85%. Hepatocytes were plated on collagen-coated glass coverslips at 18,000 cells/cm^2 density with William's E medium supplemented with 5% fetal calf serum (FCS). Collagen isolated from rat tail was supplied by Sigma Chemical Co. (St. Louis, Missouri). Twenty-four hours after plating, some cells were processed right away for tubulin visualization and formed the "negative control" set. Some more were exposed to the fungicide Benomyl™ (ICI Soplant S.p.A., 98% purity) dissolved in dimethylsulphoxide (DMSO: 1% v/v final concentration) at a given concentration and for a given time and formed the various "treated" sets. The "recovery" experiment consisted of replacing the Benomyl™-contaminated medium by the standard one and letting the culture incubate for 24 h more. Tubulin was made visible through the following steps. Cells were washed in phosphate-buffered saline (PBS: 136 mM NaCl, 2.6 mM KCl, 8 mM $Na_2HPO_4 \cdot 2H_2O$, 1.6 mM $NaH_2PO_4 \cdot H_2O$, pH 7.4) and fixed for 10 min at room temperature with 3% formaldehyde in PBS. After rins-

ing with PBS, cells were permeabilized first with high performance liquid chromatography (HPLC)-grade methanol then with HPLC-grade acetone both at −20 °C for a few seconds, then incubated with a blocking solution made of PBS+1% BSA for 10 min. Standard indirect immunofluorescence staining was performed: the primary anti-α-tubulin antibody (Amersham, Amersham Buks., United Kingdom) was diluted 1:100 in PBS+1%BSA and the cells incubated in a humid atmosphere for 1 h at 37 °C. After rinsing with PBS +1%BSA, fluorescent staining was performed for 45 min at 37 °C with the secondary antibody (Amersham, Amersham Buks., United Kingdom), namely, Texas Red-conjugated goat anti-mouse immunoglobulin (Ig) (1:50 in PBS+1%BSA). After the final rinsing with PBS and distilled water, the coverslips were mounted and viewed in a Zeiss Axioplan™ microscope equipped with epifluorescence optics at 630× magnification and a numerical aperture of 1.40 in oil. The filter set consisted of the bandpass BP 546 tuned for excitation wavelengths ranging from 540 to 552 nm, a bandstop FT 580, a dichroic beamsplitter and a lowpass LP 590, which transmits fluorescence radiation at 590 nm and higher. Photographs were taken with Kodak T-max 400™ film.

All epifluorescence images were digitized at a resolution of 700 dpi (27.5 dots per mm) and saved in BMP, 8-bit gray scale format such that 0 corresponded to black and 255 to white, as a consequence they had the same magnification (551×). Since spectral analysis relied on the discrete Fourier transform (Sec. 5.5), square tiles had to be cut out of the original images by supplying the upper left corner coordinates to the image readin function. The size of a tile was 512 ×512 pixels. Original images usually contained more than one cell. Therefore, tiles were cut in such a way as to include the border areas of the cell aggregate, where microtubules were best visible in each set. This rule applied to all tiles except the one labeled X (Fig. 6 in Sec. 6.4), taken from the perinuclear region of an untreated cell. In that area, the organization of microtubule bundles could not be evaluated; context-independent visual observation was insufficient to tell whether the image came from a control cell or from a treated one, regardless of dose.

4 Classifier Specifications and Design

4.1 Required Morphological Descriptors

Since experiments were carried out in different situations, the average fluorescence yield affecting a given image varied. Moreover, the photograph sets of a given experiment were developed and printed at different times. As a consequence, images had to be analyzed by methods exhibiting the least possible sensitivity to the average fluorescence intensity and to the absolute relation between exposure and film density.

The features to be extracted from the images for classification had to translate into quantitative terms those properties that a human expert believes to characterize cytoskeletal organization or loss thereof. In morphological terms, said features depend on image structure (leading features) and, to some extent, on texture (fine details).

The fully developed microtubules of a normal cytoskeleton are known to have indented contours, whereas an altered cytoskeleton has a smoother contour. One morphological de-

scriptor known to quantify indentation is the contour fractal dimension, denoted by D_{FP} (Secs. 5.2 and 6.1).

The number of microtubule bundles per unit area, i.e., the "mass density," of a normal cytoskeleton is lower than that of an altered one. A suitable descriptor, suggested, e.g., by the morphological analysis of dendritic materials,[46] is the mass fractal dimension D_{FM} (Secs. 5.3 and 6.2).

Microtubule bundles give rise to more or less visible edges in a gray-scale image. Global, direction-independent edge indicators are therefore necessary, such as the total variation (TV) and a suitable norm of the Laplace operator L. Both descriptors are computed in the direct domain, i.e., by (discrete) spatial differentiation (Secs. 5.4 and 6.3).

Finally, a set of descriptors was required that

1. are independent of the coarse (very low spatial frequency) details in the image and possibly of the absolute fluorescence intensity

2. can quantify the organization of microtubule bundles for example by (a) detecting straight or fan-shaped bundles regardless of their direction and (b) discriminating straight bundles (typical of a normal cytoskeleton) from curly ones (caused e.g., by treatments)

3. include the contribution from weakly emitting although structured microtubule bundles far away from the MTOC

4. quantify "structure" as compared to "texture" of the image, e.g., in terms of relative power spectral densities.

Separation of image structure from texture is one of the fundamental tasks of image understanding, which was formalized by the Osher-Rudin paradigm (Chap. 1 of Ref. 47). In this application, structure observed in a cytoskeleton is due to organized microtubule bundles, whereas (straight or curly) isolated tubules and image noise contribute to texture. The diameter of a microtubule is 25 nm. If straight bundles are formed by, say, 5 to 20 microtubules, the image will contain structures of spatial period ranging from 250 to 1000 nm. The corresponding fundamental spatial frequency will range from 4 to 1 cycles/μm. Hence the analysis of the power spectrum shall be tuned to that frequency domain.

The implementation of these requirements by means of "spectrum enhancement" is described in Secs. 5.5 and 6.4. Note also that Table 1 summarizes the symbols used in this paper.

4.2 Classification Experiment Design

The classification experiment was designed to implement all three stages, i.e., training, validation and recognition. Figure 1 provides examples of the image types and an outline and Table 2 the complete list of processed tile sets. Untreated cells, which underwent all sample preparation stages described in the previous section except exposure to Benomyl™, served as negative control: they yielded comparable images divided into the C and C_V tile sets for experimental purpose. The $T502h$ and $T502h_V$ sets were derived from treatment with Benomyl™ at experimental conditions (50 μg/ml for 2 h) classified as "extreme" according to the morphological and biochemical evidence given by Ref. 3. Cells from intermediate treatments gave rise to other tile sets, e.g., $T2530$ (25 μg/ml for 30 min). Cells from 24-h recovery after the $T502h$ treatment yielded the R tile set. The C and $T502h$ sets were used for classifier training (Sec. 7) as well as

the X tile (Sec. 3 and Fig. 6 in Sec. 6.4). The C_V and $T502h_V$ tiles were used for classifier validation (Sec. 8). Sets $T5015$, $T5030$, $T252h$, and $T2530$ were used in the recognition stage to rank the effects of intermediate concentrations and exposure times on morphology (Sec. 9.1). The analysis of set R is presented in Sec. 9.2.

5 Methods of Morphological Analysis

An image is conveniently modeled by the discrete counterpart of a nonnegative function $g(\mathbf{x})$ of position $\mathbf{x}$ with support in the open set Ω, the tile.

5.1 Preprocessing and Optimal Thresholding

Given the heterogeneity of experimental conditions and of photographic processing (Sec. 4.1), independence of the absolute fluorescence intensity could be achieved by normalizing the gray-scale histogram of each tile separately. Histogram normalization is an affine transformation of $g(\mathbf{x})$ into $f(\mathbf{x})$ according to

$$g(\mathbf{x}) \rightarrow f(\mathbf{x}) = \alpha g(\mathbf{x}) + \beta \geq 0 \text{ in } \Omega, \qquad (1)$$

where α and β depend on the specific tile.

The extraction of a few morphological descriptors required image thresholding, e.g., for binarization or background subtraction. Several methods exist that determine a binary threshold according to some optimality criterion. In this paper, the optimum threshold for each tile τ was determined to maximize cross-correlation $\rho_{g\gamma}(t)$ between the original gray scale g and the black-and-white image $\gamma(t)$ binarized according to the threshold t. Formally,

$$\tau := \underset{0 \leq t \leq s_{max}}{\arg \max} [\rho_{g\gamma}(t)]. \qquad (2)$$

The algorithm, described by Kindratenko,[48] is reported in Appendix A. Adaptive methods that determine position-dependent thresholds were not implemented to avoid introducing statistical heterogeneity between images.

5.2 Contour Fractal Analysis

The purpose of contour fractal analysis is to estimate the corresponding fractal dimension D_{FP}. A typical algorithm consists of the following eight stages: (1) τ thresholding (Sec. 5.1); (2) determination of the Férét diameter F_D; (3) contour tracking; (4) estimation of the perimeter $P(y)$ by different values of the yardstick y; ranging from $y = (1/2)F_D$ to $y = 1$ pixel; (5) contour correction wherever applicable; (6) construction of the $\log[P(y)]$ versus $\log(y)$ Richardson plot; (7) determination of the morphological threshold y_{MT}; and (8) linear interpolation of the plot in $1 \leq y \leq y_{MT}$. Some of the computer algorithms can be found in Ref. 48.

As shown in Appendix B, Proposition 1, the value of D_{FP} estimated from an image binarized by the τ of Eq. (2) is invariant with respect to affine transformations of $g(\cdot)$ such as histogram normalization [Eq. (1)]. As a consequence D_{FP} is an intrinsic property of the analyzed tile, not affected by absolute gray levels.

Table 1 List of symbols.

Symbol	Meaning	Symbol	Meaning
$\gamma(t)$	Binarized image	F_D	Feret diameter
Γ	Set centroid	$g(x)$	Gray-scale image
δ	DIRAC measure	$h(u)$	Enhanced spectrum
η	Background threshold	I	Axis of inertia
θ	Polar angle	J	Dimension of Princ. Component space
Θ	Arc of integration	K	Number of classes
μ_n	Sample mean	ℓ	Pixel size
$\rho_{g\gamma}(t)$	Cross-correlation	L	Tile side
σ_n	Sample standard deviation	L_η	Laplacian norm
τ	Optimum threshold	M	Number of tiles
Ω	Spatial domain	$m^{(p)}$	Spectrum model
A	Area under the curve	MTOC	Microtubule organizing center
b_1, b_2	Branches of a Spanning Tree	N	Number of descriptors
$C, C_V, \hat{C}$	Control sets	p	Model exponent
c	Average curvature	$P(y)$	Perimeter
d	Polynomial degree	PCA	Principal component analysis
$\mathcal{D}$	Morphological descriptor set	q	Interpolating polynomial
$\mathbf{D}_1$, and $\mathbf{D}_2$	Discriminant functions	$Q[.]$	Flop-flip reflection
DA	Discriminant analysis	q_R	Degree of recovery
d_{CT}	Distance between centroids	R	Recovery set
D_{FM}	Mass fractal dimension	$\mathfrak{R}$	Rectangle in principal component plane
D_{FP}	Contour fractal dimension	$s(u)$	Averaged spectral density
$\mathcal{T}$	Surface of the torus	SL_η	Averaged Laplacian
$\mathbf{T}$	Projection matrix	V_K	Information content
$T252h$	25 μg Benomyl/ml, 2-h set	$\mathbf{w}_m$	Vector in principal component Space
$T2530$	25 μg Benomyl/ml, 30 min set	X	Outlier tile
$T5015$	50 μg Benomyl/ml, 15 min set	$\mathbf{x}$	Position vector
$T502h, \hat{T}$	50 μg Benomyl/ml, 2-h sets	$\mathbf{X}$	Raw feature matrix
$T502h_V$	50 μg Benomyl/ml, 2-h validation set	y	Yardstick
$T5030$	50 μg Benomyl/ml, 30 min set	$\mathbf{Y}$	Feature matrix
TV_η	Total variation	$\mathbf{y}_m$	Feature vector
u	Wave number	z	Principal component

Table 2 Image sets forming the experiment design.

Tile Set	Benomy™ Concentration (μg/ml)	Exposure Time (hh:mm)	Recovery Time (hh:mm)	Remarks	Number of Tiles	Section
C X	NA	NA	NA	training control set (Fig. 1, top): includes the perinuclear tile, X (Fig. 6)	$8(C) + 1(X)$ (see text)	8
C_V	NA	NA	NA	validation control set [Fig. 9(a)]	8	9
$T502h$	50	2:00	0:0	training treated set: extreme treatment (Fig. 1, left)	8	8
$T502h_V$	50	2:00	0:0	validation treated set [Fig. 9(b)]	8	9
$T5015$	50	0:15	0:0	damage ranking set	22	9.1
$T5030$	50	0:30	0:0	damage ranking set	6	9.1
$T252h$	25	2:00	0:0	damage ranking set	7	9.1
$T2530$	25	0:30	0:0	damage ranking set (Fig. 1, right)	20	9.1
R	50	2:00	24:00	damage ranking set: treatment, then recovery in control medium (Fig. 1, bottom)	12	9.2

NA stands for not applicable.

5.3 Mass Fractal Analysis

Among the methods that estimate the mass fractal dimension D_{FM}, box counting[46] is the most straightforward. It also operates on a binarized image and relies on regression of a Richardson plot. Details are left to the implementation (Sec. 6.2).

5.4 Direct Methods (Spatial Differentiation)

Although all methods are applied to a discrete context, a continuum setting now simplifies the description. By assuming

$$g \in W^{2,1}(\Omega), \tag{3}$$

the Sobolev space of functions absolutely integrable in Ω together with their derivatives up to the second, the following subdomain was defined

$$\Omega_\eta := \{\mathbf{x} \in \Omega \,|\, g(\mathbf{x}) \geqslant \eta\}, \tag{4}$$

where η is a suitable threshold. Heuristically, η is an estimate of peak background noise, hence $g(\mathbf{x})$ in Ω_η is above such noise level. The Ω_η averaged total variation

$$\text{TV}_\eta = \frac{1}{|\Omega_\eta|} \|\nabla g\|_1, \tag{5}$$

and 1 norm of the Laplacian,

$$L_\eta = \frac{1}{|\Omega_\eta|} \|\nabla^2 g\|_1, \tag{6}$$

where $|\Omega_\eta|$ is the area of Ω_η, can serve as direction-independent edge indicators, as specified in Sec. 4.1. Obviously, they are affected by affine gray-scale transformations. By letting $\sigma = \alpha\eta + \beta$ [Eq. (1)], where η is directly proportional to τ of Eq. (2), and defining $\Omega_\sigma := \{\mathbf{x} \in \Omega \,|\, f(\mathbf{x}) \geqslant \sigma\}$,

then $|\Omega_\sigma| = |\Omega_\eta|$ and one can immediately verify that the norms scale according to

$$\|\nabla f\|_1 = |\alpha| \|\nabla g\|_1 \text{ and } \|\nabla^2 f\|_1 = |\alpha| \|\nabla^2 g\|_1. \tag{7}$$

5.5 "Spectrum Enhancement"

The spectrum enhancement algorithm, suggested by the experimental results from a coherent optical image processor many years ago[49] and specifically developed[41,50–53] for image classification in the past 3 yr, meets all the specifications listed in Sec. 4.1.

Let $Q\Omega$ denote a square of side-length L and consider an image, i.e., a function $Qg(\mathbf{x})$, $\mathbf{x} \equiv \{x_1, x_2\} \in Q\Omega$, which is continuous on the surface $\mathcal{T}$ of the torus obtained by glueing the opposite sides of $Q\Omega$ together. One way of obtaining such a $Qg(\cdot)$ from an image $g(\cdot)$ defined in a square tile Ω of side-length $L/2$ is the application of the twofold $Q(\cdot) = \text{flop}[\text{flip}(\cdot)]$ reflection. Next let $Q\Omega$ be discretized by a square grid of step-length ℓ. Let $\mathbf{u} \equiv \{u_1, u_2\}$ be the spatial frequency vector. Then the discrete Fourier transform $G(\mathbf{u})$ of $Qg(\cdot)$ is defined in the square

$$0 \leqslant |u_1|, \quad |u_2| \leqslant u_{\max} = L/2\ell - 1 \text{ cycles/image}. \tag{8}$$

In the implementation below $L = 1024$ pixels, corresponding to 26 μm, hence,

$$u_{\max} = 511 \text{ cycles/image} \equiv 19{,}650 \text{ cycles/mm}. \tag{9}$$

As a consequence of the continuity of $Qg(\cdot)$ on $\mathcal{T}$, $G(\mathbf{u})$ exhibits no "cross-artifact" (e.g., Chap. 4 of Ref. 46).

Represent $\mathbf{u}$ in polar coordinates $\mathbf{u} \equiv \{u, \theta\}$, where $u = |\mathbf{u}|$ is the wave number, and θ is the polar angle such that $0 \leqslant \theta \leqslant 2\pi$. Denote by $|G(\mathbf{u})|^2$ the power spectral density. Due to

the symmetry of $Qg(\cdot)$, the main axes of inertia of $|G(\mathbf{u})|^2$ (those that diagonalize the inertia tensor) coincide with $\mathbf{u}_1$ and $\mathbf{u}_2$. Let Θ denote an arc symmetric with respect to either axis. Then the normalized, arc-averaged spectral density profile is the function $s(\cdot)$ of u alone defined in $0 \leqslant u \leqslant u_{max}$ (cycles/image) according to

$$s(u) = \frac{1}{|\Theta|} \int_{\Theta} 10 \log_{10}\left[\frac{|G(\mathbf{u})|^2}{|G(\mathbf{0})|^2}\right] u \mathrm{d}\theta, \qquad (10)$$

where $|\Theta|$ is the length of Θ, and obviously $|G(\mathbf{0})|^2 \neq 0$ for any nondegenerate image. The value of $|\Theta|$ is provided in Sec. 7.

Let $m(u)$ be a model spectral density. For example, choose

$$m^{(p)}(u) = 0, \quad 0 \leqslant u \leqslant 1; \quad m^{(p)}(u) = -10 \log_{10}(u^p),$$
$$u \geqslant 1 \text{ cycles/image}, \qquad (11)$$

where $p(>0)$ is the model exponent. Then the enhanced spectrum $h(u)$ is defined by

$$h(u) = s(u) - m^{(p)}(u), \quad 1 \leqslant u \leqslant u_{max}. \qquad (12)$$

Intuitively, the function $h(\cdot)$ represents deviations of $s[\cdot]$ from a given model.

Among the properties of the enhanced spectrum $h[u]$ the following two are worth mentioning.

Proposition 2. In the interval $0 \leqslant u \leqslant u_{max}$, $h(u)$ is invariant with respect to scaling transformations such that $\beta = 0$ in Eq. (1), applied to the gray levels of the input image.

This is a straightforward consequence of normalization [Eq. (10)]. As a result, the enhanced spectrum reflects the intrinsic properties of the analyzed tile.

The second property is a relation between $h(\mathbf{u})$ and spatial differentiation of $Qg(\mathbf{x})$.

Proposition 3 (in words). When $p/2$ is an integer, the enhanced spectrum corresponds to evaluating all spatial derivatives of order $p/2$ of the image, taking their Fourier transforms, forming a linear combination of the squared moduli, adding $\delta(u)$, taking the logarithm and averaging over Θ. The formal statement and other remarks are provided in Appendix C.

From a practical point of view, conversion of $|G(\mathbf{u})|^2$ to the log scale [Eq. (10)] amplifies the contribution of structured but weakly emitting microtubules. Averaging over Θ makes $s(u)$ independent of bundle direction. Comparison between the asymptotics of the given power spectrum and a model of the $m^{(p)}(\cdot)$ class has been implied by previous studies involving visual processing.[54] The emphasis herewith is on the low-frequency behavior of $h(\cdot)$ for example in $1 \leqslant u \leqslant (1/4)u_{max}$, aimed at enhancing image structure and assessing the relative weight of texture. Given the scale factor of Eq. (9), the approximate spatial frequency range to which microtubule bundles shall contribute most in terms of power spectral density is

$$20 < u < 100 \text{ cycles/image}. \qquad (13)$$

The spectrum enhancement code was based on the fast Fourier transform and singular value decomposition taken from Ref. 55 and on additional authors' own feature extraction
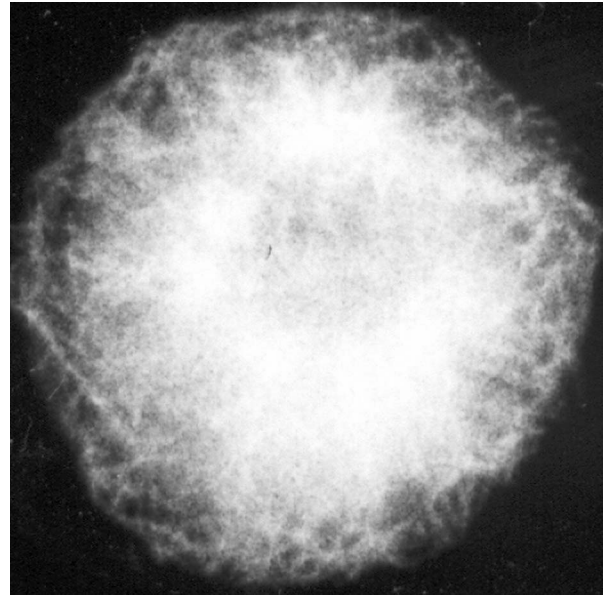

Fig. 3 Microtubules of a treated cell, tile be502_ 04. Square side length=13 μm.

functions. It was written in C and run in conjunction with other pieces of software.

6 Extraction of Morphological Descriptors

6.1 *Contour Fractal Dimension D_{FP}*

Contour correction, step 5 of Sec. 5.2, consisted of subtracting from $P(y)$ the y independent length of the straight segments along the boundary of the square before building the Richardson plot. Otherwise D_{FP} would have been underestimated. The threshold y_{MT} (step 7) was determined once for all from the Richardson plot of a contour of known dimension. This is a yardstick value that separates the structural part (large y, highly oscillatory graph) of the plot from the textural one (small y, smoother graph). The Richardson plots yielded by the tiles of Figs. 2 and 3 are shown by Fig. 4. Contour correction was applied to the former plot. The latter tile, instead, which showed a whole cytoskeleton, did not need any correction. The estimated values of D_{FP} for C tiles, including that of Fig. 2, were affected by the deep contour indentations due to filaments. The smoother contours of *T502h* tiles (Fig. 3) yielded lower values, as expected.

6.2 *Mass Fractal Dimension D_{FM}*

The D_{FM} was estimated by box counting[46] on each previously normalized and τ binarized tile. The software used was Benoit™ 1.3 of TruSoft Inc.[56] Typically, the box scaling ratio was 1.3 and the grid orientation angle was stepped by 15 deg.

The values of tile set-averaged D_{FP} and D_{FM} and their standard deviations are shown in Table 3.

6.3 *Total Variation TV_η and Laplacian Norm L_η*

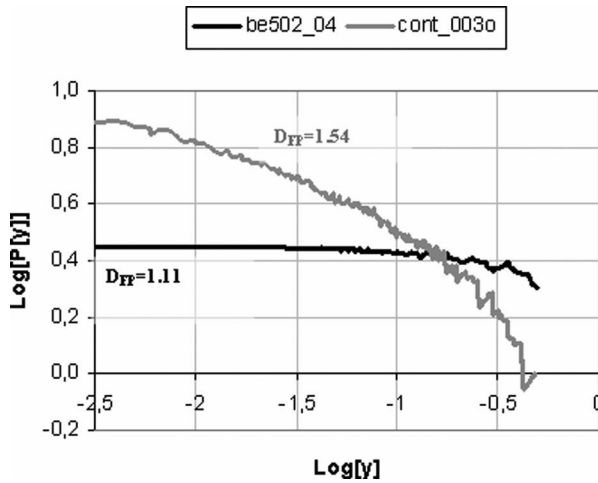The relation between τ and η mentioned at the end of Sec. 5.4 was

Fig. 4 Richardson plots related to contour fractal analysis. All length values in units of the Férét diameter. For plot cont_03o, derived from Fig. 2, estimated $D_{FP}=1.54$ after discounting for straight edges, and for plot be502_04 derived from Fig. 3, estimated $D_{FP}=1.11$. No straight-edge correction was required.

Fig. 5 Interpolated enhanced spectra of representative tiles used in classifier training. Integration is about the major axis of inertia over an arc of ±46 deg; model exponent $p=1.8$; degree of polynomial $d=9$. Plots cont_1a and cont_3b represent the C set, plots be502_1a and be502_3a represent the $T502h$ set; and plot cont_x is the perinuclear tile (see Fig. 6). Local maxima in the spatial frequency range $20<u<100$ cycles/image correspond to structured microtubule bundles of a normal cytoskeleton.

$$\eta = 0.8\tau, \qquad (14)$$

where the coefficient 0.8 was found during classifier training (Sec. 7). The set-averaged values of TV_η and L_η and their standard deviations are listed by Table 3. The signed, domain-averaged Laplacian $SL_\eta = (1/|\Omega_\eta|)\int_{\Omega_\eta}\nabla^2 f\, d\Omega$ was used in early training attempts (Sec. 8.1) and later dismissed.

6.4 Descriptors of the Enhanced Spectrum

From here on the wave number is assumed to be discrete and span the interval $0 \leq u \leq u_{max}$. The enhanced spectrum can be regarded as the signature of a given tile, and as such, the graph $\{u, h(u)\}$ is an array of first-level morphological descriptors. The decisi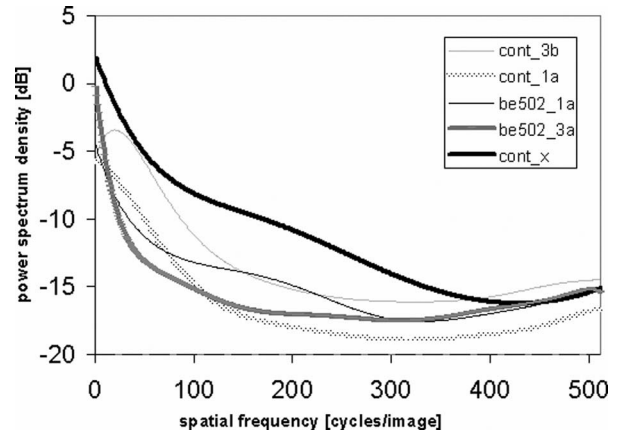on was made to extract fewer second-level descriptors according to some criterion. For any exponent p, $h(u)$ exhibits a trend over which jumps and oscillations are superimposed. In fact, the latter are amplified with respect to those of $s(\cdot)$. For this reason the value $h(0)=0$ was reassigned according to $h(0) \leftarrow h(1)$ and $h(\cdot)$ was interpolated in $0 \leq u \leq u_{max}$ by a polynomial $q(\cdot; d)$ of suitable degree d. Four parameters eventually affected $q(\cdot; d)$: the axis of inertia ($I=1$: major axis, $I=2$: minor axis) about which integration was carried out [Eq. (10)], the arc Θ, the model exponent p, and the degree d.

Plots obtained from some tiles used in classifier training with $I=1$, $|\theta| \leq 46$ deg, $p=1.8$, and $d=9$ are shown in Fig. 5. In agreement with the estimate of Eq. (13), enhanced spectra

Table 3 Set averages of descriptors used by the implemented classifier.

Set	D_{FP}	D_{FM}	TV_η	L_η	A	$q'(0)$	c
C	1.49(±0.05)	1.78(±0.03)	6.84(±0.52)	7.82(±0.96)	51.72(±0.59)	0.167(±0.43)	0.762(±0.711)
X	1.31	1.82	6.51	60.45	−68.40	−0.199	−0.598
C_V	1.43(±0.04)	1.84(±0.04)	6.28(±0.62)	6.48(±0.74)	52.50(±96.88)	0.125(±0.23)	0.864(±0.16)
$T502h$	1.32(±0.11)	1.88(±0.05)	5.75(±0.60)	7.12(±0.89)	−141.84(±0.78)	−0.352(±0.63)	−1.188(±0.36)
$T502h_V$	1.34(±0.10)	1.818(±0.40)	5.29(±0.70)	6.29(±0.99)	−243.01(±127.76)	−0.618(±0.39)	−0.704(±0.94)
$T5015$	1.45(±0.10)	1.83(±0.40)	5.37(±0.70)	5.84(±0.99)	−45.37(±0.99)	−0.059(±0.39)	0.351(±0.94)
$T5030$	1.36(±0.07)	1.84(±0.04)	6.15(±0.49)	7.37(±0.89)	−206.13(±21.41)	−0.470(±0.29)	−0.652(±0.33)
$T252h$	1.32(±0.07)	1.87(±0.02)	6.29(±0.56)	7.96(±0.51)	−187.20(±27.70)	−0.451(±0.35)	−0.629(±0.92)
$T2530$	1.34(±0.11)	1.82(±0.07)	6.77(±0.74)	8.61(±1.14)	−159.32(±146.56)	−0.384(±0.39)	−0.936(±0.65)
R	1.40(±0.60)	1.81(±.61)	5.52(±1.25)	4.99(±2.18)	55.82(±0.87)	0.193(±0.45)	0.897(±1.18)

Units of measurement, wherever defined, are omitted, Standard deviations are shown between parentheses. D_{FP}, D_{FM}, TV_η, and L_η are strictly positive, whereas A, $q'(0)$, and c can be negative, zero or positive.
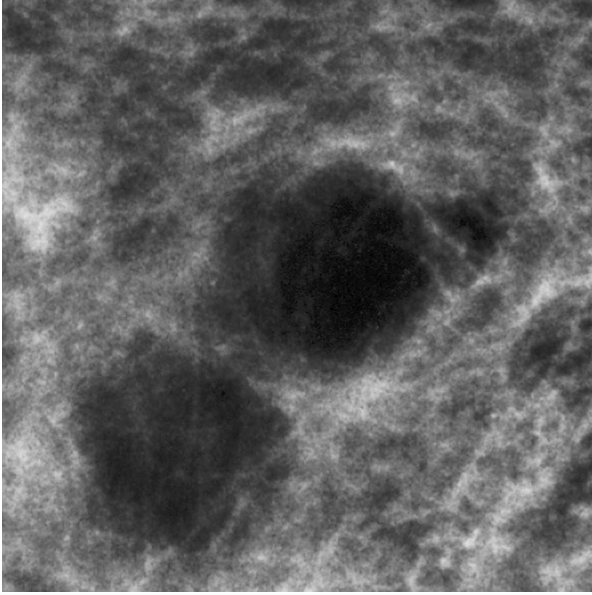
Fig. 6 Perinuclear tile X cut from a control image. Context-free classification of this tile is impossible, even to a human expert. It is classified as an outlier (Sec. 7).

from the C set generally exhibited a local maximum in $0 < u < 63$ cycles/image as shown, e.g., by cont_3b (Fig. 5). One exception was tile cont_1a. None of the $T502h$ tiles (plots be502_3a and be502_1a of Fig. 5) had such maximum; in fact, $q'(\cdot) < 0$ in the same frequency range. The plot cont_x of the perinuclear tile X seemed to deviate from all other plots of either set. Tile X itself is shown in Fig. 6.

The selection of second-level descriptors was a part of classifier training (Sec. 7) and initially involved the following five quantities:

1. $A = \int_0^{u_H} [q(u) - q(0)] du$, a signed area under the curve, where $u_H = 15$ cycles/image

2. $q'(0)$, the first derivative of $q(\cdot)$ at the origin,

3. $c = -(1/u_C) \int_0^{u_C} \{q'(u)/[1 + q'(u)^2]^{3/2}\} du$, the opposite of the average curvature of the graph in $0 \leqslant u \leqslant u_C$, where $u_C = u_{\max}/2$

4. $q''(0)$, the second derivative of $q(\cdot)$ at the origin

5. $\operatorname{argmax}_1(q)$, the abscissa of the first proper maximum of $q(\cdot)$, if any, in $0 \leqslant u \leqslant u_C$.

The values of u_H and u_C were also determined in the training stage. As one can infer from the last three columns of Table 3, the first three descriptors, A, $q'(0)$, and c were eventually selected for image classification.

7 Classifier Training

The data used at this stage came from 8 C tiles, 8 $T502h$ tiles, and X, hence a total of $M = 17$ tiles were analyzed. By examining morphological descriptors one by one (univariate analysis) it was found that none of them was capable of discriminating the three classes. For example, according to $\operatorname{argmax}_1(q)$ two C tiles were clustered with the $T502h$ set. The same misclassification error was caused by choosing $q'(0)$ alone. As a consequence, descriptor fusion had to be attempted: the chosen method was principal components

analysis (PCA), which is one of the most relevant procedures in unsupervised factor extraction (e.g., Chap. 5 of Ref. 57). The goal of training was to maximize discrimination between classes in the sense to be specified in the following. This was achieved by finding optimal (or suboptimal) values of the following:

1. the number N of descriptors to use

2. the set $\mathcal{D}$ of descriptors such that card $(\mathcal{D}) = N$

3. the parameters η/τ [Eq. (14)], I, Θ, p, d, u_H, and u_C (Sec. 6)

The raw feature matrix $\mathbf{X} = [x_{n,m}]$ consisted of N rows and M columns. Each column was formed by the N descriptors of a tile. Before applying PCA the entries of $\mathbf{X}$ were normalized rowwise: the sample mean μ_n, $1 \leqslant n \leqslant N$, of each descriptor over the training set was subtracted and the difference divided by the sample standard deviation σ_n. The normalized feature (column) vectors denoted by $\mathbf{y}_m$, $1 \leqslant m \leqslant M$, formed the normalized feature matrix $\mathbf{Y}$. As is well known, PCA constructs the linear space spanned by principal components, i.e., the eigenvectors $\mathbf{z}_1, \mathbf{z}_2, \ldots$ of the covariance matrix generated from $\mathbf{Y}$. Eigenvectors are labeled after the corresponding eigenvalues, arranged in a nonincreasing sequence. Then PCA projects the $\mathbf{y}_m$s onto a subspace, the dimension of which $\mathbf{J}$ is no greater than min $\{M, N\}$. The quotient

$$V_k = 100 \frac{\sum_{j=1}^{k} \mu_j}{\sum_{j=1}^{J} \mu_j} \qquad (15)$$

is the cumulated percent variance or information content carried, or explained by the first $k(\leqslant J)$ eigenvalues. Each of the M tiles is represented by a J-dimensional vector $\mathbf{w}_m$, $1 \leqslant m \leqslant M$. For ease of interpretation the result is displayed in the plane $\{\mathbf{z}_1; \mathbf{z}_2\}$ of the first two principal components. Eventually, to each tile in the training set there corresponds a point in $\{\mathbf{z}_1; \mathbf{z}_2\}$.

Discrimination between classes C, $T502h$, and X was rated by drawing the minimum spanning tree (MST) (Ref. 58 and algorithm AS13 in Ref. 59) in $\{\mathbf{z}_1; \mathbf{z}_2\}$. The two longest branches, b_1 and b_2, of the MST by definition divide the whole set of points into three subsets, say S_1, S_2, and S_3. If each of these subsets contains points belonging to one class only, i.e., there is a one-to-one correspondence between the *a posteriori* assignment $\{S_1, S_2, S_3\}$ and the *a priori* classes of belonging $\{C, T502h, X\}$, then classification is MST-correct and as such accepted.

Optimization of the preceding items 1 to 3 was performed by running cluster analysis (e.g., Chap. 8 of Ref. 57), varying N and the parameter values within reasonable bounds, running PCA, and looking at the ordered branch list of the MST. After several attempts the following values were determined:

$$\eta/\tau = 0.8, \quad I = 1, \quad |\Theta|/u = 92 \text{ deg}, \quad p = 1.8, \quad d = 9,$$

$$N = 7, \quad u_H = 15 \text{ cycles/image}, \quad u_C = u_{\max}/2,$$

$$\mathcal{D}_7 = \{D_{\text{FP}}, D_{\text{FM}}, \text{TV}_\eta, L_\eta, A, q'(0), c\}. \qquad (16)$$

In the first place, an MST-correct classification was attained: b_1 joined X to a C tile, thus classifying X as an "outlier."
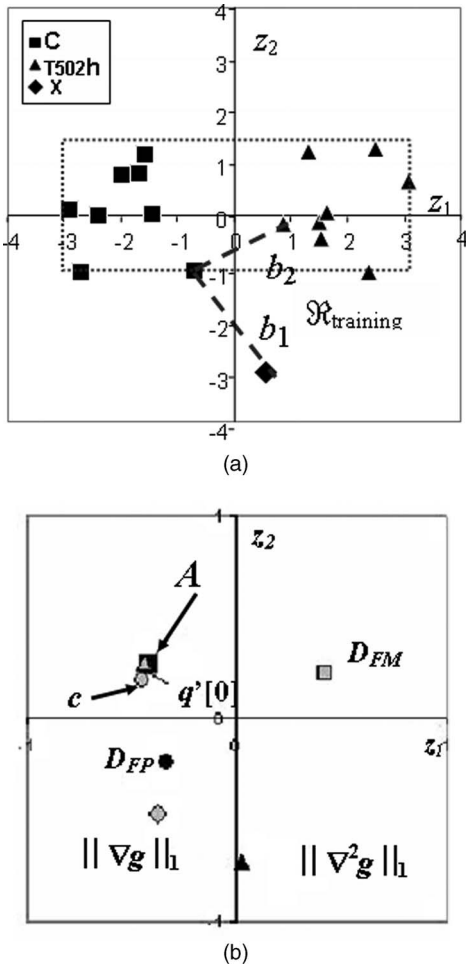
(a)

(b)

Fig. 7 (a) Training set represented in the $\{\mathbf{z}_1;\mathbf{z}_2\}$ principal plane, where C set, filled boxes; $T502h$ set, filled triangles; X (diamond), the perinuclear tile; and b_1 and b_2, two longest branches of the MST. The spread of both the C and the $T502h$ sets along $\mathbf{z}_1$ is slightly larger than that along $\mathbf{z}_2$. The first principal component explains 58% of the sample variance, the first two together explain 75% and the first three 89%; $\mathfrak{R}_{\text{training}}$, rectangle circumscribed to the tiles. (b) Factor loadings of the seven morphological descriptors extracted by the methods of Sec. 6. Four descriptors ($D_{\text{FP}},A,c,q'(0)$) correlate negatively with z_1 and are less correlated to z_2. The total variation TV_η is more negatively correlated with z_2 than with z_1. Mass fractal dimension D_{FM} is positively correlated with z_1. The Laplacian L_η is highly anticorrelated with z_2 and uncorrelated to z_1. The two fractal dimensions carry independent pieces of information, whereas a high mutual correlation characterizes the three spectral descriptors A, $q'(0)$, and c.

Moreover, the distance d_{CT} between the set centroids Γ_C and Γ_{T502h} was found to be $d_{\text{CT}}=3.78$ and the fractions of explained variance were $V_1=58\%$, $V_2=75\%$, and $V_3=89\%$. Since $N<M$ it was decided to let $J=N$ and to form the $N\times2$ matrix

$$\mathbf{T}=[\mathbf{z}_1\ \mathbf{z}_2] \qquad (17)$$

to be used later in validation (Sec. 8.2) and recognition (Sec. 9). The classification result is shown by Fig. 7(a), where the rectangle circumscribed to the training tiles,
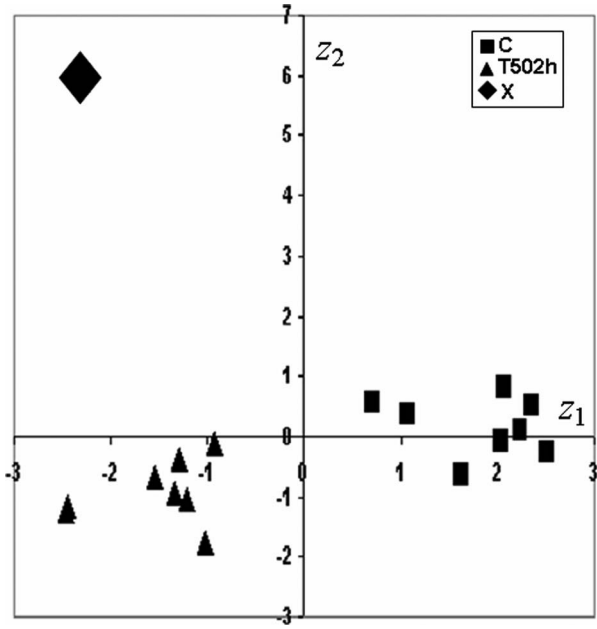

Fig. 8 Classification of the C set (filled boxes), the $T502h$ set (filled triangles), and $X(^*)$ by descriptor set $\mathcal{D}_8$. Modulo reflections of both axes, the pattern is similar to that of Fig. 7(a), in spite of the different number ($N=8$ instead of 7) and list of descriptors [Eq. (19) instead of Eq. (16)]. Note the different scales of $\mathbf{z}_1$ and $\mathbf{z}_2$. The first principal component explains 41% of the sample variance, the first two together explain 75%, and the first three 87%.

$$\mathfrak{R}_{\text{training}}=\{-3\leqslant z_1\leqslant3.1,-1\leqslant z_2\leqslant1.4\}, \qquad (18)$$

is drawn.

The factor loadings of the morphological descriptors are shown by Fig. 7(b). The caption carries some comments. Factor loadings provide, in part, the morphological interpretation of the principal components themselves and justify the position of some tiles in $\{\mathbf{z}_1;\mathbf{z}_2\}$. For example, X stands out for its high L_η, therefore it will lie in the lower half-plane far away from the origin. All C tiles have a larger D_{FP}, therefore they will end up in the left half-plane. All $T502h$ tiles have a larger D_{FM}, and are therefore located in the right half-plane. Those C tiles that have larger A, c, and $q'(0)$ lie in the second quadrant. All of these deductions are easily verified by inspecting Fig. 7(a).

PCA was carried out by SPSS™ (Statistical Package for the Social Sciences), version 11.

8 Classifier Sensitivity and Validation

8.1 Sensitivity to Descriptors

In an early training attempt,[44] the set

$$\mathcal{D}_8=\{D_{\text{FP}},D_{\text{FM}}^{127},\text{TV}_\eta,L_\eta,SL_\eta,\ \text{argmax}_1(q),q'(0),c\},$$
$$(19)$$

such that $N=8$, was formed by using the same parameters as in the first line of Eq. (16), with one exception: D_{FM}^{127} was computed at the fixed binary threshold, 127. The resulting representation in $\{\mathbf{z}_1;\mathbf{z}_2\}$ is shown by Fig. 8. Classification was MST-correct and yielded $d_{\text{CT}}=3.52$. More comments are

Table 4 Indicators of classifier sensitivity with respect to descriptor sets.

Descriptor Set	$\dfrac{\text{dist}(C, T502h)}{d_{CT}}$	$\dfrac{\text{diam}(C)}{d_{CT}}$	$\dfrac{\text{diam}(T502h)}{d_{CT}}$
$\mathcal{D}_8$	0.52	0.58	0.58
$\mathcal{D}_7$	0.50	0.73	0.66

Note d_{CT} serves as a yardstick in the $\{\mathbf{z}_1 ; \mathbf{z}_2\}$ plane. Classifier sensitivity to descriptors has to be assessed in relative, not absolute, terms. In going from $\mathcal{D}_8$ to $\mathcal{D}_7$ the normalized distance between clusters. [dist$(C, T502h)/d_{CT}$] (column 2), in almost unchanged, whereas the normalized diameters [diam$(.)/d_{CT}$] of both clusters C (column 3) and $T502h$ (column 4) increase by 26 and 13% respectively. One can conclude that the classifier is relatively "stable," Details are provided in the text.

provided in the figure caption. The factor loadings also exhibited a pattern that, modulo reflections of both axes, resembled that of Fig. 7(b).

The sensitivity of the classification to changes in the descriptor sets (from $\mathcal{D}_8$ to $\mathcal{D}_7$) can be now quantified as follows. The set $\mathcal{D}_7$ differs from $\mathcal{D}_8$ by three descriptors out of eight. The situation in $\{\mathbf{z}_1 ; \mathbf{z}_2\}$ can be summarized by the following quotients: $[\text{dist}(C, T502h)/d_{CT}]$, $[\text{diam}(C)/d_{CT}]$, and $[\text{diam}(T502h)/d_{CT}]$, where dist$(\cdot,\cdot)$ is the distance between two clusters (minimum distance between two points belonging to either cluster), diam$(\cdot)$ is the diameter of a cluster, and d_{CT} serves as a yardstick in the $\{\mathbf{z}_1 ; \mathbf{z}_2\}$ plane. The values are given by Table 4. Ideally $[\text{dist}(C, T502h)/d_{CT}]$ would be close to 1, and the other two will be much smaller than 1. Neither $\mathcal{D}_8$ nor $\mathcal{D}_7$ provide the "ideal" classification. However, the focus is on classifier sensitivity: therefore, a comparison between $\mathcal{D}_8$ and $\mathcal{D}_7$ has to be made in relative terms. The normalized distance between clusters $[\text{dist}(C, T502h)/d_{CT}]$ is almost insensitive to the descriptor set: this means sets C and $T502h$ are as "separable" by $\mathcal{D}_7$, as they were by $\mathcal{D}_8$. Instead, the normalized diameters $[\text{diam}(\cdot)/d_{CT}]$ of both clusters C and $T502h$ are more sensitive to the replacement of $\mathcal{D}_8$ by $\mathcal{D}_7$, because they increase by 26 and 13%, respectively; $\mathcal{D}_7$ makes both training sets look "more heterogeneous" than they were under $\mathcal{D}_8$. From this numerical experiment, one can conclude that the classifier is relatively "stable." Further evidence of classifier "stability" is provided by the values of V_k, $k=1,2,3$, given in the caption of Fig. 8; the first three principal components derived from either $\mathcal{D}_8$ or $\mathcal{D}_7$ carry the same amount of information.

8.2 Internal Validation

Internal validation consisted of submitting to the trained classifier some new tiles belonging to either class, then projecting the corresponding feature vectors onto $\{\mathbf{z}_1 ; \mathbf{z}_2\}$ by means of **T** of Eq. (17) and finally computing sensitivities and specificities.

In detail, the 8 C_V and 8 $T502h_V$ tiles defined in Sec. 4 were selected from boundary areas of the available images. Unlike those used in training, some C_V and $T502h_V$ tiles could not be easily classified visually. For example Figs. 9(a) and 9(b) exhibit "borderline" morphologies; at the top right of Fig. 9(a), near the cell nucleus, is a dense mass of tubulin,
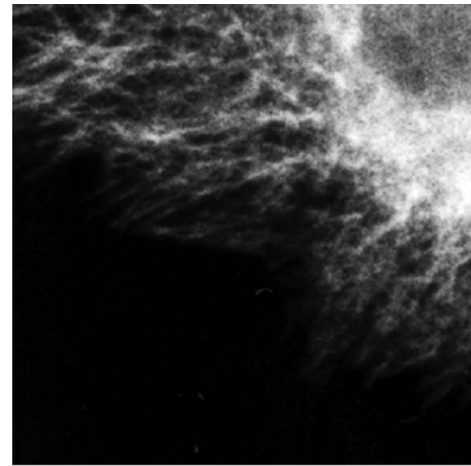
(a)
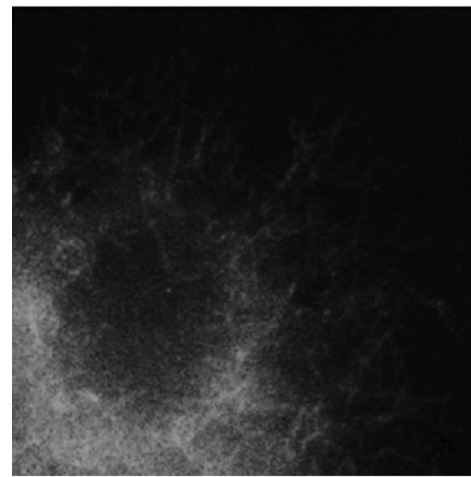
(b)

Fig. 9 (a) Tile of the C_V validation set, where the dense, poorly structured microtubules on the upper right, close to the perinuclear region, look treated. Misclassification is expected, as shown in Fig. 10(b). Square side length=13 μm. (b) Tile of the $T502h_V$ validation set, where microtubules on the boundary, although randomly oriented, exhibit sufficient structure as in a control cytoskeleton. Misclassification is expected, as shown in Fig. 10(b). Square side length=13 μm.

which looks disorganized, whereas the boundary tubules of Fig. 9(b) are sufficiently structured as in a control cytoskeleton.

Descriptors were extracted by the procedure outlined in Sec. 7. By assumption, the training tiles represented their respective sets, therefore normalization consisted of subtracting the μ_n and dividing by the σ_n computed in the preceding. The normalized feature vectors $\mathbf{y}_m$, $1 \leq m \leq M = 16$, were determined for each tile of the validation sets. The $\mathbf{y}_m$s were projected onto $\{\mathbf{z}_1 ; \mathbf{z}_2\}$ according to

$$\mathbf{w}_m = \mathbf{T}^{\text{Trs}} \cdot \mathbf{y}_m. \qquad (20)$$

The validation result in terms of centroids is displayed by Fig. 10(a). The relevant distances between centroids are $d_{CC_v} = 1.12$ and $d_{TT_v} = 0.424$, which can provide the confidence bounds of subsequent recognition results. In relative terms,
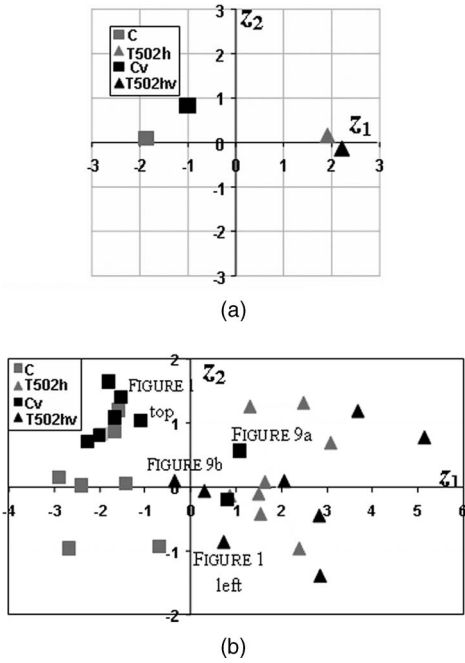
(a)

(b)

Fig. 10 (a) Centroids of the training sets $\{C, T502h\}$ (gray) and of the validation sets $\{C_V, T502h_V\}$ (black). The displacement of the $T502h_V$ centroid with respect to the $T502h$ centroid is relatively small. (b) Validation result. Tiles of the C_V set are represented by filled boxes, those of the $T502h_V$ set by filled triangles. Training tiles (Sec. 7) are shown by gray boxes and triangles respectively. Not all C_V tiles are on the left half-plane as well as not all $T502h_V$ tiles are on the right one.

using d_{CT} as a yardstick again, the quotients $d_{CC_v}/d_{CT}=0.30$ and $d_{TT_v}/d_{CT}=0.11$ quantify the "stability" of the classifier.

In terms of individual tiles the result is shown by Fig. 10(b). References to a few images are also displayed. The diameters of both C_V and $T502h_V$ clusters are larger than those of C and $T502h$. Two C_V tiles, one of which is Fig. 9(a), are positioned closer to the $T502h$ set and one $T502h_V$ tile [Fig. 9(b)] is closer to the C set. The z_1 coordinates of these three tiles [Fig. 10(b)], which deviate from those of the remaining tiles, can be explained by means of the z_1 loadings of the morphological indicators [Fig. 7(b)]. For example, the tile of Fig. 9(b) has $D_{FP}=1.475$, the highest value in the $T502h_V$ set, comparable to the C and C_V set averages (Table 3). Since D_{FP} is negatively correlated to z_1, this property suffices to position the tile in the left half-plane. About the C_V tile of Fig. 9(a), its enhanced spectrum, like that of a $T502h$ tile, has no local maximum. The presence or absence of the latter affects all three indicators A, $q'(0)$, and c, which negatively correlate to z_1. Therefore, this tile shall lie away from the centroid of the C-(training) set and possibly in the right half-plane.

Table 5 Sensitivity and specificity of the classifier in validation mode.

Set	Sensitivity (%)	Specificity (%)
C	75	86
$T502h$	87	77

Table 6 Sensitivity and specificity obtained from discriminant analysis.

Set	Sensitivity (%)	Specificity (%)
$\hat{C}$	87	100
$\hat{T}$	100	89

If $\{\mathbf{z}_1; \mathbf{z}_2\}$ is regarded as a feature plane, then inspection of Fig. 10(b) suggests the training sample is separable; there is a straight line, e.g., $z_1=-0.036$, that divides the C and $T502h$ sets. Each tile of the validation set could be classified accordingly. The confusion matrix was formed and the sensitivity and specificity values of Table 5 were obtained.

8.3 Discriminant Function Analysis

Classification is said to be supervised whenever the class to which a feature vector belongs is known beforehand. Given K classes, discriminant analysis (DA for short; e.g., Chap. 3 of Ref. 57) implements supervised classification by looking for $K-1$ affine combinations, called discriminant functions, of the N features (the morphological descriptors), which maximize separation between classes and minimize within-class scatter. Three classes of belonging were defined: (1) the singleton X, (2) $\hat{C}$ made of 8 C and 8 C_V tiles, and (3) $\hat{T}$ made of 8 $T502h$ and 8 $T502h_V$ tiles, hence $M=33$. The corresponding $N \times M$ raw feature matrix was normalized rowwise as in Sec. 7 and DA carried out both by SPSS™ and by the LDA module of Q-Parvus.[60] The 3×3 classification (or "confusion") matrix $\mathbf{K}$ was constructed. Since 14 $\hat{C}$ tiles were assigned to the $\hat{C}$ class and 2 to the $\hat{T}$ class, whereas X and all $\hat{T}$ tiles were correctly classified, the relevant sensitivity (normalized row-wise sums of entries of $\mathbf{K}$) and specificity (normalized column-wise sums of entries of $\mathbf{K}$) of Table 6 resulted. A cutout of the $\{\mathbf{D}_1; \mathbf{D}_2\}$ discriminant functions plane is shown by Fig. 11. For the purpose of classifier training and
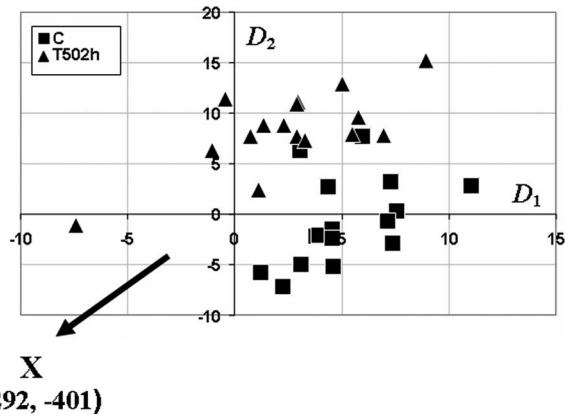

X
(-292, -401)

Fig. 11 Discriminant analysis where the $\hat{C}$ and $\hat{T}$ sets are made of training and validation tiles together; $\hat{C}$ (boxes) and $\hat{T}$ (triangles) tiles are represented in a plane where the discriminant functions $\{\mathbf{D}_1; \mathbf{D}_2\}$ form the reference frame. The X tile is located further away from the origin.

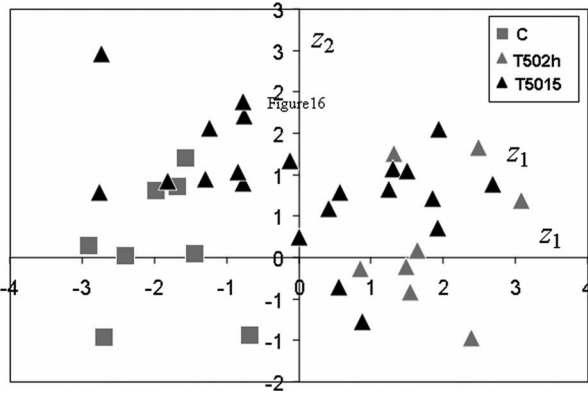**Fig. 12** *T5015* tiles (filled triangles) in the $\{z_1; z_2\}$ plane. Tiles derived from exposure to 50 μg/ml for 15 min. Training *C* (gray boxes) and *T502h* tiles (gray triangles) are shown for reference.

Fig. 13 Tiles *T2530* (filled disks) in the $\{z_1; z_2\}$ plane. Tiles derived from exposure to 25 μg/ml for 30 min. Training *C* (gray boxes) and *T502h* tiles (gray triangles) are shown for reference. As compared to *T252h* tiles, *T2530* tiles are more scattered. Some are closer to the *C* half-plane. The tile placed at the extreme left exhibited the typical microtubule structure of a control cytoskeleton.

validation, DA answers the question of how suitable are the given morphological descriptors to discriminate between the given *K* classes.

Sensitivities and specificities shall all be greater than 50%, regardless of *K*. In the ideal case, they are all equal to 100%, which corresponds to a diagonal **K**. From the entries of Table 6 one deduced that information stored in the chosen descriptor set, $\mathcal{D}_7$, could adequately and reliably tell $\hat{C}$ from $\hat{T}$ tiles, a necessary condition for going over to the next, more challenging tasks: recognizing and ranking tiles from other experiments.

9 Quantitative Estimates of Structural Damage and Recovery

The *T5015*, *T5030*, *T252h*, *T2530*, and *R* sets were submitted to the trained classifier with the aim of representing their elements in $\{z_1; z_2\}$ and, in case of sensible results, quantifying cytoskeletal organization. Feature vectors were normalized and projected onto $\{z_1; z_2\}$, as in Sec. 8.2.

9.1 Effects of Different Treatments

Projection onto $\{z_1; z_2\}$ scattered the *T5015* tiles almost evenly in the rectangle $\{-2.7 \leq z_1 \leq 2.8, -0.9 \leq z_2 \leq 3.0\}$, as shown by Fig. 12. Their centroid lay at $\Gamma_{T5015} \equiv \{-0.082, 0.924\}$. Tiles of the *T5030* set (Fig. 9 of Ref. 45) were mostly aggregated in the *T502h* area. Their centroid lay at $\Gamma_{T5030} \equiv \{1.529, -0.362\}$.

Classification of tiles derived from exposure at 25 μg/ml is represented by Fig. 13, which pertains to the *T2530* set. Comments are included in the caption. Results for the *T252h* set were reported in Fig. 10 of Ref. 45. The centroid coordinates were $\Gamma_{T252h} \equiv \{1.714, -0.215\}$ and $\Gamma_{T2530} \equiv \{1.028, -0.721\}$, respectively.

9.2 Quantitative Estimate of Structural Recovery after Treatment

Undisputable experimental evidence[3] showed that cytoskeletal structures are capable of recovering after exposure to toxic substances, provided that dose does not exceed some threshold. Visual inspection of *R* images (Sec. 3) suggested that cytoskeletal damage had to be reversible, at least in part.
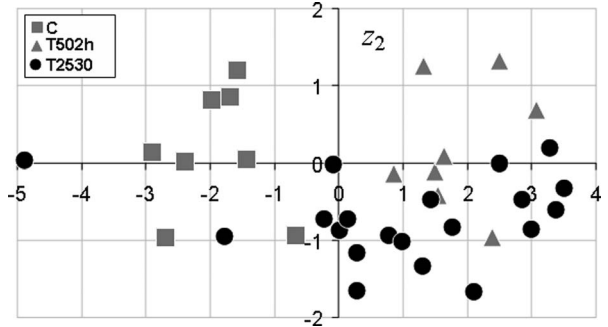
The first quantitative result about structural recovery was obtained by the $\mathcal{D}_8$ classifier (Ref. 44 and Sec. 8.2). Herewith, the $\mathcal{D}_7$ classifier (Sec. 7) was applied to the *R* tiles and yielded the result of Fig. 14. Only 3 out of 12 tiles are located in the *T502h* half-plane and the remainder in the *C* half-plane.

From the z_1 coordinates of centroids, $z_{1,T502h}$, $z_{1,R}$, and $z_{1,C}$ one can form the quotient

$$q := \frac{z_{1,R} - z_{1,T502h}}{z_{1,C} - z_{1,T502h}}, \tag{21}$$

and estimate tile-set-averaged cytoskeletal organization therefrom. Namely, $z_{1,C}$ corresponds to normal structure and to a fully functional cytoskeleton ($q=1$), whereas $z_{1,T502h}$ corresponds to the most severe damage of the whole experimental design ($q=0$). From Eq. (21),

$$q = 0.73^{+0.18}_{-0.07}, \tag{22}$$

where the worst case confidence interval has been determined from the spread of the centroid z_1 coordinates (Sec. 8.2). The estimate compares to 0.77, determined by the $\mathcal{D}_8$ classifier.[44] This may be regarded as further evidence of classifier stability in the recognition mode.
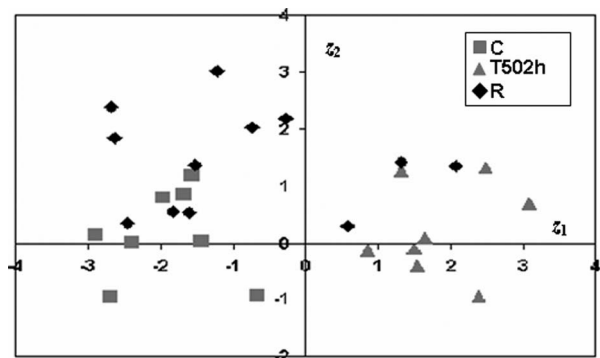

Fig. 14 Tiles *R* (filled diamonds) in the $\{z_1; z_2\}$ plane. This result provides evidence of 0.73 (+0.18, −0.07) structural recovery 24 h after extreme treatment (50 μg/ml for 2 h). Tiles *C* and *T502h* are shown for reference.
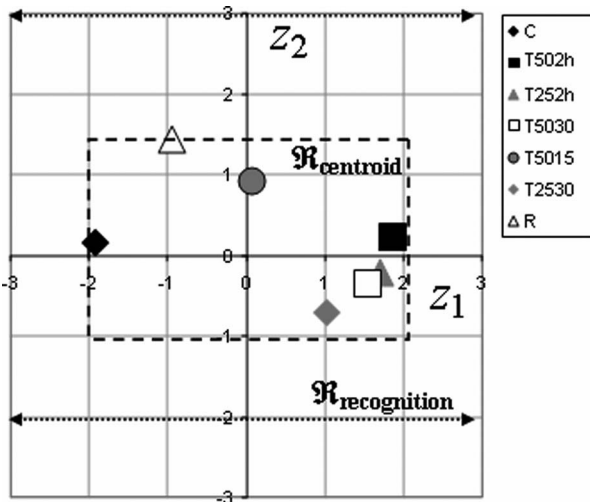
Fig. 15 Set centroids, where $\mathfrak{R}_{\text{centroid}} = \{-2 \leq z_1 \leq 2, -1 \leq z_2 \leq 1.5\}$ = rectangle containing the centroids and $\mathfrak{R}_{\text{recognition}} = \{-5 \leq z_1 \leq 3.5, -2 \leq z_2 \leq 3\}$ = rectangle circumscribed to all classified tiles. Comments are provided in Sec. 10.3. The X tile is not shown.

9.3 Ranking by Centroids

To summarize the results, the centroids of all sets, except those used in validation, are displayed by Fig. 15. According to the z_1 coordinate alone, the sets form the sequence

$$C, \quad R, \quad T5015, \quad T2530, \quad T5030, \quad T252h, \quad T502h, \tag{23}$$

where the order of the last three terms shall not be taken for final, because the confidence bounds of Sec. 8.2 apply.

10 Discussion

The relevance of microtubule dynamics in living cells and the sensitivity of cytoskeletal organization to anticancer drugs, xenobiotics, and pathological conditions have provided the basic motivation for this paper. Further motivation at the practical level has come from the abundance of images of cytoskeletal microtubules obtained during previous experiments.[3] In general, the heterogeneity of biological response and the variability of experimental results even under controlled conditions pose a challenge to quantitative classification by simplistic methods intended to support and/or replace visual assessment. The latter has been the only way to judge the degree of cytoskeletal organization for a long time. However, conclusions have always been influenced by the operator.

10.1 Image Formation, Capture, and Analysis

All images were obtained from an ordinary epifluorescence microscope, acquired from photographic film developed and printed after each experiment. Therefore,

1. The intensity of the exciting radiation need not have been uniform.

2. The image represented a 3-D object.

3. Fluorescence intensity was converted into film transmittance with batch-dependent parameters.

On one hand, the wide dynamic range of film obviously was an advantage because it made weakly emitting microtu-

bules visible. On the other hand, parameter variability would have prevented classification based on absolute fluorescence values. The threshold of Eq. (2) (which implies Proposition 1, Appendix B) and the spectrum enhancement algorithm of Secs. 5.5 and 6.4 (to which Proposition 2 applies) were selected as countermeasures for 1 and 2.

The opportunity of replacing ordinary by confocal microscopy in the morphological analysis of the cytoskeleton is still a matter of discussion; in Ref. 38, confocal images were successfully processed; however, there are situations[61] where ordinary microscopy has been more informative.

In principle the whole procedure, from analysis to classification, can be applied to images acquired by different microscopes and sensors.

10.2 Meaning of Some Morphological Descriptors

The estimated values of the fractal dimensions D_{FP} and D_{FM} agree with expectations (Sec. 4.1) and are easily interpreted accordingly. Fully developed microtubules of the control set do have indented contours (higher D_{FP}) and lower mass density (D_{FM}). The loss of organization caused by treatment (sets $T502h$, $T252h$, and R) yields a more compact cytoskeleton (higher D_{FM}) with a smoother contour (lower D_{FP}).

The two descriptors from direct methods (Secs. 5.4 and 6.3) are linked to visual properties of images. For example, the well organized microtubules of C cells (Fig. 2) suggest a higher value of total variation TV_η than that of $T502h$ cells (Fig. 3), which is in agreement with Table 3. The norm of the Laplacian, L_η, is uncorrelated to z_1 [Fig. 7(b)] and uniquely characterizes X: microtubules around the MTOC, hence in tile X, appear entangled under an ordinary, nonconfocal microscope, and as such do not exhibit any symmetry. This justifies the very large L_η of X and the anticorrelation of L_η to z_2. If classes are ranked by increasing TV_η one obtains the following sequence (Table 3)

$$T5015, \quad R, \quad T502h, \quad T5030, \quad T252h, \quad T2530, \quad C. \tag{24}$$

Similarly, ranking by L_η yields

$$R, \quad T5015, \quad T502h, \quad T5030, \quad C, \quad T252h, \quad T2530. \tag{25}$$

Both TV_η and L_η have thus determined the positioning of the $T2530$ centroid in the lower half-plane and of the R and $T5015$ centroids in the upper one. However, a detailed explanation of how microtubule arrangement affects TV_η and L_η remains beyond reach.

In spectrum enhancement (Secs. 5.5 and 6.4) the subtraction of $m^{(p)}$ [Eq. (11)] was the key feature of the algorithm. Namely, the subtraction of $m^{(p)}(\cdot)$ from $s(\cdot)$ [Eq. (12)] represents the deviation of $s(\cdot)$ from the proposed asymptotics. Moreover, polynomial interpolation reduced the sensitivity of morphological indicators to the oscillations of $h(\cdot)$. Separation of structure from texture is context dependent. In this application the values of either $h(\cdot)$ or $q(\cdot)$ in the interval $0 \leq u \leq 63$ cycles/image (approximately 2500 cycles/mm in the case of Figs. 2 and 3) represented image structure, whereas those in $63 \leq u \leq u_{\max}/2$ corresponded to those textural de-

tails, which contributed to classification. In particular, local maxima of $q(\cdot)$ in $0 \leq u \leq 63$ cycles/image were originated by high contrast bundles of microtubules, typical of control cells, not observed in damaged cytoskeletal proteins (Fig. 3). Since the selected degree of $q(\cdot)$ is relatively low ($d=9$), it is obvious that a local maximum to the right of the origin correlates with both $A>0$ and $q'(0)>0$. If said maximum is peaked enough, then the c of Sec. 6.4 is positive (lines C and C_V of Table 3). In the sets $T502h$ and $T502h_V$ all three descriptors have opposite signs. The simultaneous occurrence of these properties explains why A, and $q'(0)$ have very close factor loadings [Fig. 7(b)].

The angle-averaged spectra shown in Refs. 36 (logarithmic intensity scale) and 37 (linear scale) can be compared to $s(\cdot)$ of Eq. (10). They do exhibit local maxima even without enhancement.

The remarks in this section should help in justifying the classification result of Fig. 7(a).

10.3 Overall Classifier Performance

The statistical significance of the described classification results is supported by the following arguments and figures. Section 8 provided the necessary evidence of classifier "stability" and validity for continuing on to applications. Recognition of a relatively large set of new tiles (67) in Sec. 9 were essentially an extended validation test of a classifier trained by a total of $M=17$ tiles: namely, the R, $T5015$, $T2530$, $T5030$, and $T252h$ centroids (Fig. 15) all belong to the rectangle $\mathfrak{R}_{\text{centroid}} = \{-2 \leq z_1 \leq 2, -1 \leq z_2 \leq 1.5\}$, i.e., they fall within the strip $\{-2 \leq z_1 \leq 2\}$ defined by the C and $T502h$ centroids after training. Moreover, none of the recognized tiles falls outside the rectangle $\mathfrak{R}_{\text{recognition}} = \{-5 \leq z_1 \leq 3.5, -2 \leq z_2 \leq 3\}$ and 46 out of 67, i.e., 68.6% fall within $\mathfrak{R}_{\text{training}}$ of Eq. (18). These results should not be taken for granted and prove that training based on a set of 17 tiles has captured enough of cytoskeletal morphology.

The correspondence between the gross *a priori* threefold distinction

{no treatment}

∪ {intermediate treatments} ∪ {extreme treatment},

and the *a posteriori* ranking of centroids (Fig. 15) has been established in terms of $\mathbf{z}_1$, which explains 58% of the sample variance.

10.4 Innovative Features

All image analysis methods quoted in Sec. 2 represented significant advances toward automated classification. However, each of them relied on only one type of morphological descriptor. Instead, this paper implemented the fusion of heterogeneous morphological descriptors: fractal analysis, direct methods, and spectrum enhancement together have led to the fingerprint of an image.

Moreover, spectrum enhancement is a relatively new algorithm. It was introduced by the first author and so far it has been successfully applied to classify scattering patterns[50] and electron microscope images of other materials such as ceramic nanoaggregates[51,52] and tire tread particles.[53] Its first application to images of cytoskeleta was presented in Ref. 41.

The third innovative feature of this paper is the application of the trained classifier to rank structural damage and quantify recovery.

10.5 Possible Developments

Although multivariate statistics is a standard tool in image classification and pattern recognition, feature extraction remains task specific and deserves additional effort. Therefore, some improvements could be brought in to increase classifier throughput and to speed up the learning phase:

1. automated image tiling, intended to replace the selection of tiles by user supplied coordinates (Sec. 3)

2. automated selection of descriptors out of a predefined set followed by the tuning of control parameters (Sec. 7 and 8)

3. the inclusion of more descriptors which have immediate morphological and functional meaning, as those used by Refs. 39 and 40.

On the applications side, the analysis of image sets coming from different experiments on different cell lines would outline the "operating region" of the whole approach.

11 Conclusion

Images of cytoskeletal microtubules obtained from the immunofluorescence microscopy of primary culture rat hepatocytes were processed. Contour and mass fractal analysis, direct methods, and spectrum enhancement were designed and tuned to make the extracted morphological descriptors insensitive to absolute fluorescence intensities. Data fusion for classification was achieved by means of multivariate analysis. Validation was supplemented by discriminant functions analysis. Finally, the classifier was applied to ranking structural damage and quantifying recovery.

The innovative features of the classifier described here, other than the application of spectrum enhancement, are the concurrent implementation of different analysis methods, the fusion of morphological descriptors by multivariate statistics, and the application of the classifier to images from various experiments.

Differences in cytoskeletal morphology were translated into the selected descriptors. The procedure developed and implemented here may lead to automatic image recognition. Namely, the method can become a tool for testing cytotoxicity and for extracting quantitative information about intracellular alterations of various origins.

Appendix A

The optimum threshold τ is defined as follows. Let the image be the discrete counterpart of a nonnegative function $g(\mathbf{x})$ of position $\mathbf{x}$ with support in the open set Ω, the tile, which takes values in the interval $0 \leq s \leq s_{\max}$. Denote by t a threshold, $0 \leq t \leq s_{\max}$, and by $\gamma(t)$ the t binarized image. Let p_s denote the relative frequency by which the gray level of g is s and define the below and above threshold means $m_0(t)$, $m_1(t)$, of $\gamma(t)$ according to

$$m_0(t) = \sum_{s=0}^{t} sp_s \left\{ \sum_{s=0}^{t} p_s \right\}^{-1}, \quad m_1(t) = \sum_{s=t+1}^{s_{max}} sp_s \left\{ \sum_{s=t+1}^{s_{max}} p_s \right\}^{-1}.$$

(26)

Next define the first- and second-order moments of $g(\cdot)$ and $\gamma(t)$:

$$E_g := \sum_{s=0}^{s_{max}} sp_s,$$

$$E_{gg} := \sum_{s=0}^{s_{max}} s^2 p_s, \quad E_\gamma := \sum_{s=0}^{t} m_0(t) p_s + \sum_{s=t+1}^{t_{max}} m_1(t) p_s,$$

$$E_{\gamma\gamma} := \sum_{s=0}^{t} m_0^2(t) p_s + \sum_{s=t+1}^{t_{max}} m_1^2(t) p_s,$$

$$E_{g\gamma} := \sum_{s=0}^{t} s m_0(t) p_s + \sum_{s=t+1}^{t_{max}} s m_1(t) p_s,$$

(27)

and let

$$V_g := E_{gg} - (E_g)^2 \text{ and } V_\gamma := E_{\gamma\gamma} - [E_\gamma(t)]^2.$$

(28)

The cross-correlation function of t is defined by

$$\rho_{g\gamma}(t) := [E_{g\gamma}(t) - E_g E_\gamma(t)]/[V_g V_\gamma(t)]^{1/2}.$$

(29)

As a consequence the optimum threshold τ is the value that maximizes $\rho_{g\gamma}(t)$ [Eq. (2)].

Appendix B

Proposition 1. D_{FP} is invariant with respect to affine transformations of $g(\cdot)$ defined by Eq. (1).

Proof. Let $v = \alpha\tau + \beta$ be the transformed threshold, ϕ denote the v binarized counterpart of f, and let E_f, E_ϕ, E_{ff}, $E_{f\phi}$, and $E_{\phi\phi}$ denote the corresponding moments. By applying the affine transformation of Eq. (1) it is immediate to show that the moments relate by

$$E_f = \alpha E_g + \beta, \quad E_{ff} = \alpha^2 E_{gg} + 2\alpha\beta E_g + \beta^2,$$

$$E_{f\phi} = \alpha^2 E_{g\gamma}(\tau) + \alpha\beta[E_g + E_\gamma(\tau)] + \alpha\beta E_\gamma(\tau),$$

(30)

and so forth. As a consequence the standard deviations of Eq. (28), scale according to

$$V_f = \alpha^2 V_g, \quad V_\varphi(v) = \alpha^2 V_\gamma(\tau),$$

(31)

and therefore the correlations can be shown to comply with

$$\rho_{f\varphi}(v) = \rho_{g\gamma}(\tau).$$

(32)

Finally, the subdomains $\Omega_\tau := \{x \in \Omega \,|\, g(x) \geqslant \tau\}$ and $\Omega_v := \{x \in \Omega \,|\, f(x) \geqslant v\}$ satisfy

$$\Omega_v = \Omega_\tau.$$

(33)

Since $\partial\Omega_v = \partial\Omega_\tau$, i.e., the contours are the same, one concludes that the estimated contour fractal dimensions coincide.

Appendix C

Let $\delta[\cdot - \mathbf{u}_{l,m}]$ be the Dirac measure supported at integer coordinates

$$(l,m) = (0,0), (\pm 1, 0), (0, \pm 1), \ldots, (\pm u_{max}, \pm u_{max}), \quad (34)$$

in the $\mathbf{u}$ plane. As a consequence of periodicity, the Fourier transform of $Qg(\mathbf{x})$ is the tempered distribution

$$G(u) = \sum_{l,m} a_{l,m} \delta(\mathbf{u} - \mathbf{u}_{l,m}),$$

(35)

with the ranges of l and m specified by Eq. (34). The integral over Θ of Eq. (10) therefore is understood as a sum over the grid nodes where the distribution is supported. The normalized power spectral density derived from Eq. (35) is

$$\frac{|G(\mathbf{u})|^2}{|a_{0,0}|^2} = \sum \frac{|a_{l,m}|^2}{|a_{0,0}|^2} \delta(\mathbf{u} - \mathbf{u}_{l,m}).$$

(36)

Proposition 3 (formally). Assume the image is not degenerate, the derivatives of $Qg(\cdot)$ up to a suitable order exist as tempered distributions and the model exponent satisfies $p/2 = N(>0)$, integer.

1. Then the enhanced power spectral density defined by

$$H(\mathbf{u}) = |\mathbf{u}|^p \frac{|G(\mathbf{u})|^2}{|a_{0,0}|^2} + \delta(\mathbf{u}),$$

(37)

where $|\mathbf{u}|^p = (u_1^2 + u_2^2)^{p/2}$, complies with

$$H(\mathbf{u}) = \frac{1}{|a_{0,0}|^2} \sum_{n=0}^{N} \binom{N}{n} \left| \mathcal{F}\left[\frac{\partial^N Qg}{\partial^{(N-n)} x_1 \partial^n x_2} \right] \right|^2 + \delta(\mathbf{u}). \quad (38)$$

2. Moreover, if all Fourier coefficients satisfy

$$|a_{l,m}|^2 \geqslant \varepsilon > 0,$$

(39)

then the function of Eq. (12) complies with

$$h(u) = \frac{10}{|\Theta|} \int_\Theta \log_{10}[H(\mathbf{u})] u \, d\vartheta.$$

(40)

Statement 1 is proved by means of the differentiation theorem applied to distribution-valued Fourier transforms (e.g., Sec. 74 of Ref. 62). Statement 2 follows from the properties of tempered distributions.

If $p/2$ is not an integer, $H(\mathbf{u})$ can be related to a pseudo-differential operator (ΨDO) acting on $Qg(\cdot)$.

References

1. H. C. Joshi, "Microtubule dynamics in living cells," *Curr. Opin. Cell Biol.* **10**, 35–44 (1998).
2. A. Lambrechts, M. van Troys, and C. Ampe, "The actin cytoskeleton in normal and pathological cell motility," *Int. J. Biochem. Cell Biol.* **36**, 1890–1909 (2004).
3. C. Urani, E. Chiesara, P. Galvani, L. Marabini, A. Santagostino, and M. Camatini, "Benomyl affects the microtubule cytoskeleton and the glutathione level of mammalian primary cultured hepatocytes," *Toxicol. Lett.* **76**, 135–144 (1995).
4. C. Urani, E. Brambilla, A. Santagostino, and M. Camatini, "1-Methyl-4-phenyl-1,2,3,6-tetrahydropyridine (MPTP) affects the actin cytoskeleton and calcium level of Swiss 3T3 mouse fibroblasts," *Toxicology* **91**, 117–126 (1994).
5. D. M. Toivola and J. E. Eriksson, "Toxins affecting cell signalling and alteration of cytoskeletal structure," *Toxicol. in Vitro* **13**, 521–530 (1999).
6. G. Bellomo and F. Mirabelli, "Oxidative stress and cytoskeletal alterations," *Ann. N.Y. Acad. Sci.* **663**, 97–109 (1992).
7. M. Marinovich, "The role of actin in the transduction of toxic effect," *Pharmacol. Res.* **24**, 319–336 (1991).
8. W. Li, Y. Zhao, and I.-N. Chou, "Alterations in cytoskeletal protein sulphydryls and cellular glutathione in cultured cells exposed to cadmium and nickel ions," *Toxicology* **77**, 65–79 (1993).
9. M. Camatini, P. Bonfanti, A. Colombo, C. Urani, and S. Crippa, "Cellular and molecular targets of benzo[a] pyrene and metal toxicity in *Xenopus laevis* embryos and in HepG2 cells," *ATLA* **27**, 325–337 (1999).
10. Y. Zhao, W. Li, and I.-N. Chou, "Cytoskeletal perturbation induced by herbicides, 2,4-dichlorophenoxyacetic acid (2,4-D) and 2,4,5-trichlorophenoxyacetic acid (2,4,5-T)," *J. Toxicol. Environ. Health* **20**, 11–26 (1987).
11. I.-N. Chou, W. Li, and G. B. Zamansky, "Fluorescence microscopic examination of cytoskeletal elements," in *Methods in Toxicology*, C. A. Tyson and J. M. Frazier, Eds., pp. 81–95, Academic Press, San Diego, CA (1994).
12. J. F. Nagelkerke, B. van de Water, I. M. Twiss, J. P. Zoetewey, H. J. G. M. de Bont, P. Dogterom, and G. Mulder, "Role of microtubuli in secretion of very-low-density lipoprotein in isolated rat hepatocytes: early effects of thiol reagents," *Hepatology (Philadelphia, PA, U. S.)* **14**, 1259–1268 (1991).
13. J. Savory, Y. Huang, M. M. Herman, and M. R. Wills, "Quantitative image analysis of temporal changes in tau and neurofilament proteins during the course of acute experimental neurofibrillary degeneration; non-phosphorylated epitopes procede phosphorylation," *Brain Res.* **707**, 272–281 (1996).
14. A. Andrieux, P. A. Salin, and D. Job, "Un rôle pour les microtubules dans les pathologies psychiatriques?" *Pathol. Biol.* **52**, 89–92 (2004).
15. M. Zaffaroni, "Biological indicators of the neurodegenerative phase of multiple sclerosis," *J. Neurol. Sci.* **24**, S279–S282 (2003).
16. J. Y. Rao, R. E. Hurst, W. D. Bales, P. L. Jones, R. A. Bass, L. T. Archer, and G. P. Hemstreet, "Cellular F-actin levels as a marker for cellular transformation: relationship to cell division and differentiation," *Cancer Res.* **50**, 2215–2220 (1990).
17. V. M. Y. Lee, "Disruption of the cytoskeleton in Alzheimer's disease," *Curr. Opin. Neurobiol.* **5**, 663–668 (1995).
18. P. M. Checchi, J. H. Nettles, J. Zhou, J. P. Snyder, and H. C. Joshi, "Microtubule-interacting drugs for cancer treatment," *Trends Pharmacol. Sci.* **24**, 361–365 (2003).
19. K. W. Wood, W. D. Cornwell, and J. R. Jackson, "Past and future of the mitotic spindle as an oncology target," *Curr. Opin. Pharmacol.* **1**, 370–377 (2001).
20. M. A. Jordan and L. Wilson, "Microtubules and actin filaments: dynamic targets for cancer chemotherapy," *Curr. Opin. Pharmacol.* **10**, 123–130 (1998).
21. M. A. Jordan and L. Wilson, "Microtubules as a target for anticancer drugs," *Nature Rev.* **4**(4), 253–265 (2004).
22. http://www.cytokinetics.com.
23. P. Geladi, H. Isaksson, L. Lindqvist, S. Wold, and K. Esbensen, "Principal components analysis of multivariate images," *Chemom. Intell. Lab. Syst.* **5**, 209–220 (1989).
24. J. P. Marques de Sá, *Pattern Recognition*, Springer, Berlin (2001).
25. P. A. Dufort and C. J. Lumsden, "Cellular automation model of the actin cytoskeleton," *Cell Motil. Cytoskeleton* **25**, 87–104 (1993).
26. L. Edelstein-Keshet and G. B. Ermentrout, "A model for actin-filament length distribution in a lamellipod," *J. Math. Biol.* **43**, 325–355 (2001).
27. M. A. Aon and S. Cortassa, "Coherent and robust modulation of a metabolic network by cytoskeletal organization and dynamics," *Biophys. Chem.* **97**, 213–231 (2002).
28. M. A. Aon and S. Cortassa, "On the fractal nature of cytoplasm," *FEBS Lett.* **344**, 1–4 (1994).
29. M. A. Aon, S. Cortassa, and D. Lloyd, "Chaotic dynamics and fractal space biochemistry: simplicity underlies complexity," *Cell Biol. Int.* **24**, 581–587 (2000).
30. L. M. Lifshitz, "Tracking cells and subcellular features," Chap. 8 in *Advances in Image Analysis*, Y. Mahdavieh and R. C. Gonzalez, Eds., pp. 218–243, SPIE Press, Bellingham, WA (1992).
31. D. B. Thomason, O. Anderson III, and V. Menon, "Fractal analysis of cytoskeleton rearrangement in cardiac muscle during head-down tilt," *J. Appl. Physiol.* **81**, 1522–1527 (1996).
32. W. J. Karlon, P. P. Hsu, S. Li, S. Chien, A. D. McCullouch, and J. H. Omens, "Measurement of orientation and distribution of cellular alignment and cytoskeletal organisation," *Ann. Biomed. Eng.* **27**, 712–720 (1999).
33. M. M. Knight, B. D. Idowu, D. A. Lee, and D. L. Bader, "Temporal changes in cytoskeletal organisation within isolated chondrocytes quantified using a novel image analysis technique," *Med. Biol. Eng. Comput.* **39**, 397–404 (2001).
34. A. M. McGough and R. Josephs, "On the structure of erythrocyte spectrin in partially expanded membrane skeletons," *Proc. Natl. Acad. Sci. U.S.A.* **87**, 5208–5212 (1990).
35. W. M. Petroll, H. D. Cavanagh, P. Barry, P. Andrews, and J. V. Jester, "Quantitative analysis of stress fiber orientation during corneal wound contraction," *J. Cell. Sci.* **104**, 353–362 (1993).
36. M. Kohler, M. Aufderheide, and D. Ramm, "Method for the description of differences in the filamentous structure of the cytoskeleton in cultured cells," *Toxicol. Lett.* **72**, 33–42 (1994).
37. V. L. Taylor and M. J. Costello, "Fourier analysis of textural variations in human normal and cataractous lens nuclear fiber cytoplasm," *Exp. Eye Res.* **69**, 163–174 (1999).
38. T. Delhaas, S. van Engeland, J. Broers, C. Bouten, N. Kuijpers, F. Ramaekers, and L. H. E. H. Snoeckx, "Quantification of cytoskeletal deformation in living cells based on hierarchical feature vector matching," *Am. J. Physiol.: Cell Physiol.* **283**, C639–C645 (2002).
39. X. Chen, M. Velliste, S. Weinstein, J. W. Jarvik, and R. F. Murphy, "Location proteomics: building subcellular location trees from high resolution 3D fluorescence microscope images of randomly tagged proteins," in *Manipulation and Analysis of Biomolecules, Cells and Tissues*, D. V. Nicolau, J. Enderlein, R. C. Leif, and D. Farkas, Eds., *Proc. SPIE* **4962**, 298–306 (2003).
40. K. Huang, M. Velliste, and R. F. Murphy, "Feature reduction for improved recognition of subcellular location patterns in fluorescence microscope images," in *Manipulation and Analysis of Biomolecules, Cells and Tissues*, D. V. Nicolau, J. Enderlein, R. C. Leif, and D. Farkas, Eds., *Proc. SPIE* **4692**, 307–318 (2003).
41. G. F. Crosta, C. Urani, and L. Fumarola, "Fourier and fractal analysis of cytoskeletal morphology altered by xeno-biotics," in *Manipulation and Analysis of Biomolecules, Cells and Tissues*, D. V. Nicolau, J. Enderlein, R. C. Leif, and D. Farkas, Eds., *Proc. SPIE* **4962**, 329–340 (2003).
42. G. F. Crosta, C. Urani, and L. Fumarola, "Morphological analysis and classification of cytoskeletal structures," in *Interdisciplinary Applications of Fractal & Chaos Theory*, R. Dobrescu and C. Vasilescu, Eds., pp. 181–195, Romanian Academy Publishing House, Bucharest (2004).
43. L. Fumarola, "Morfologia quantitativa del danno biologico su colture cellulari," MSc. Thesis, College of Sciences, Università degli Studi Milano—Bicocca, Milan (July 2003).
44. G. F. Crosta, C. Urani, and L. Fumarola, "A cytoskeletal injury classifier based on 'spectrum enhancement' and data fusion," in *Manipulation and Analysis of Biomolecules, Cells and Tissues*, D. V. Nicolau, J. Enderlein, R. C. Leif, and D. Farkas, Eds., *Proc. SPIE* **5322**, 83–94 (2004).
45. G. F. Crosta, C. Urani, and L. Fumarola, "Estimating structural damage of the cytoskeleton by means of morphological descriptors," in *Biophotonics New Frontier: From Genome to Proteome*, M. D. Faupel and P. P. Meyrueis, Eds., *Proc. SPIE* **5461**, 78–89 (2004).
46. J. C. Russ, *Fractal Surfaces*, Plenum, New York (1994).
47. Y. Meyer, *Oscillating Patterns in Image Processing and Nonlinear*

Evolution Equations—The Fifteenth Dean Jacqueline B. Lewis Memorial Lectures, AMS, Providence, RI (2001).

48. V. Kindratenko, "Development and application of image analysis techniques for identification and classification of microscopic particles," PhD Dissertation, Department of Chemistry, University of Antwerp (1997); https://netfiles.uiuc.edu/kindrtnk/www.

49. G. F. Crosta, "Texture analysis of phosphor screens," *J. Phys. E* **10**, 187–190 (1977).

50. S. Holler, S. Zomer, G. F. Crosta, Y.-L. Pan, R. K. Chang, and J. R. Bottiger, "Multivariate analysis and classification of two dimensional angular optical scattering (TAOS) patterns from aggregates," *Appl. Opt.* **43**(33), 6198–6206 (2004).

51. G. F. Crosta, C. Sung, B. Kang, C. Ospina, and P. Stenhouse, "Quantitative morphology of aluminum silicate nanoaggregates," *Mater. Res. Soc. Symp. Proc.* **738**, G.15.1–G.15.6 (2003); http://www.mrs.org/publications/epubs/proceedings/fal2002/g.

52. B. Kang, G. F. Crosta, P. J. Stenhouse, and C. Sung, "Microscopy and quantitative morphology of aluminum silicate nanoparticles grown on organic template," *J. Nanosci. Nanotechnol.* **5**(2), 334–345 (2005).

53. G. F. Crosta, G. M. Corbetta, L. Martignoni, M. C. Camatini, T. Dolukhanyan, B. Kang, C. Sung, S. Cencetti, and C. Regazzoni, "Tread abrasion, rubber degradation and the mathematical morphology of tire debris particles," in *Proc. 162nd Meeting of the Rubber Division, American Chemical Society*, pp. ACS-RD, Akron, OH (2002); http://rubber.org/applications/papersales/papersales/papers.cfm?meetingnum=162.

54. D. L. Ruderman and W. Bialek, "Statistics of natural images: scaling in the woods," *Phys. Rev. Lett.* **73**(6), 814–817 (1994).

55. W. H. Press, S. A. Teukolsky, W. T. Vetterling, and B. P. Flannery, *Numerical Recipes in C—The Art of Scientific Computing*, 2nd ed., Cambridge University Press, Cambridge, UK (1992).

56. http://www.trusoft.netmegs.com/.

57. K. Backhaus, B. Erichson, W. Plinke, and R. Weiber, *Multivariate Analysemethoden*, 10th ed., Springer, Berlin (2003).

58. R. Sedgewick, *Algorithms*, 2nd ed., Addison-Wesley, Reading, MA (1988).

59. *Appl. Stat.* **18**, 103 (1969); http://lib.stat.cmu.edu/apstat.

60. *Q-Parvus*, http://parvus.unige.it.

61. J. R. Swedlow, K. Hu, P. D. Andrews, D. S. Roos, and J. M. Murray, "Measuring tubulin content in *Toxoplasma gondii*: a comparison of laser-scanning confocal and wide-field fluorescence microscopy," *Proc. Natl. Acad. Sci. U.S.A.* **99**(4), 2014–2019 (2002).

62. C. Miranda, *Istituzioni di Analisi Funzionale Lineare*, Vol. **I**, Unione Matematica Italiana, Bologna (1978).